Modal and nonmodal stability of the laminar flow in a channel with longitudinal riblets

Antoine Jouin,[1,2] Jean-Christophe Robinet,[2] and Stefania Cherubini[1,*]
[1]*Dipartimento di Meccanica, Matematica e Management, Politecnico di Bari, Via Re David 200, 70125 Bari, Italy*
[2]*Laboratoire DynFluid, Arts et Métiers Institute of Technology, 151 Bd de l'Hopital, 75013 Paris, France*

(Received 29 January 2024; accepted 27 June 2024; published 29 July 2024)

Modal and nonmodal stability analysis of a channel flow with longitudinal riblets are investigated. To this extent, a method based on the coupling between a two-dimensional stability problem and a computational framework for n-periodic systems based on Bloch waves is proposed. Unstable modes from linear stability can be retrieved. The influence of the riblets on the most amplified flow structures is investigated through a transient growth analysis: a resonance is found when the riblet wavenumber is equal to the wavenumber of the optimal streaks in a smooth channel flow. For large riblet spacing, a wavenumber lock-in regime, in which the streaks dynamics and wavelength are totally controlled by the riblet spacing, is observed. Physically, a modulation of the streaks amplitude in the spanwise direction via a beating mechanism is seen. These phenomena are characteristic of dynamic systems spatially forced and may exhibit geometric frustration. Similar results were found in the study of secondary flows in Rayleigh-Bénard convection with wavy walls. A resolvent analysis is also performed: it is found that riblets lead to the development of oblique waves that may trigger an early transition.

DOI: 10.1103/PhysRevFluids.9.073903

I. INTRODUCTION

Surface roughness has a prominent role in the transition to turbulence and as such, has been studied since the seminal work of Reynolds [1]. The first studies were experimental [2–4] and aimed at identifying the conditions under which the roughness had an influence on the overlying turbulent flow. Specifically, the investigation of the drag-reducing properties of a rough surface has attracted a lot of attention [5–10] due to the large number of possible applications in the engineering field. The effectiveness of the drag-reducing effect was found to be dependent mostly on the roughness' spacing s with the drag reduction being a linear function of it. If the spacing increases too much, the viscous regime breaks down [8] and the rough surface increases drag instead. Several mechanisms for this breakdown were proposed: the penetration of turbulent fluctuations into the grooves [11,12] or the creation of vortices near the tips of the riblets [13]. More recently, García-Mayoral and Jiménez [7] observed the development of spanwise-coherent rollers, resulting from a Kelvin-Helmholtz instability and associated with a shear stress increase in the vicinity of the riblets. These structures were further investigated in the work of Endrikat *et al.* [14] in which the optimal roughness shape for the development of rollers was obtained.

The problem of the influence of a rough surface has also been tackled from a stability point of view by Floryan [15]. In this case, a roughness is said to be hydraulically active if it is able to induce

*Contact author: stefania.cherubini@poliba.it

flow bifurcation and transition to turbulence. This criterion requires the investigation of the linear stability of the flow over the rough surface, commonly done through a reduced order geometry (ROG) model [16]. In this framework, the roughness shape is assumed to be accurately described by the first leading modes of its Fourier expansion, which, in most cases, appear sufficient to capture the underlying physical mechanisms [17]. From there, base flows for a large variety of roughness configurations and their linear stability have been investigated, either through immersed boundary condition methods [18–20] or through domain transform approaches [19,21,22]. Depending on the flow parameters, notably on the height and wavenumber of the roughness, instabilities may arise either from traveling waves or from streamwise vortices [15]. Linear stability of the flow over longitudinal riblets was specifically investigated in the work of Moradi and Floryan [20], where quasi-two-dimensional Tollmien-Schlichting waves were found to be responsible for the transition to turbulence. Later, Mohammadi *et al.* [23] showed that Squire-related modes, located in the center of the channel, could also destabilize the flow for small streamwise wavenumbers.

All these results were obtained within the modal stability framework, focusing only on the asymptotic stability of the flow. However, due to the non-normality of the linearized Navier-Stokes operator [24], perturbations can experience a non-negligible transient energy amplification, that triggers the onset of nonlinear effects. Streaky perturbations similar to those inducing an optimal transient growth of the energy are typically observed during the laminar-turbulent transition of shear flows in subcritical conditions [25–27]. Streamwise-elongated coherent structures generated by the lift-up effect [28] are observed also in turbulent flows at both inner and outer scales, indicating that this mechanism is at the heart of the near-wall cycle [29,30], as well as at the origin of the formation of large-scale structures [31].

For several flows over hydraulically active roughnesses, the presence of non-negligible transient growth has been suggested in the experimental works of Reshotko and Leventhal [32], Corke *et al.* [33], Downs *et al.* [34] and Liu *et al.* [35]. However, to the authors' best knowledge, nonmodal stability analysis of the flow over rough surfaces has been the subject of limited research. Transient growth over a rough surface was investigated only in the works of Szumbarski and Floryan [36] for a laminar flow over a spanwise independent corrugation and in Chavarin and Luhar [10] for a turbulent flow over longitudinal riblets. The framework used in these two studies is an extension of the ROG model to transient growth computations. Moreover, a stochastic resolvent framework (surveyed in [37]) has been used by Ran *et al.* [38] to quantify the effect of longitudinal riblets on turbulent kinetic energy and skin-friction drag. Here, we propose an alternative method based on the numerical framework introduced by Schmid *et al.* [39]. This framework allows the study of the linear modal and nonmodal stability of n-periodic systems, taking into account detuned instabilities, by numerically tackling only the stability problems on a very limited number of subunits. This method has never been applied on flows over distributed wall roughnesses, but it can be easily adapted to this problem by applying a domain transform technique prior to solving the two-dimensional stability problem on the subunits, allowing both modal and nonmodal stability analyses at a reasonable cost. This method is of interest for the considered flow, since it allows one to take into account long-wavelength instabilities, which are of the order of many riblets spacings, that cannot be described by a secondary stability analysis on a single riblet. Many works (among others, see [40,41]) have shown that, under certain flow conditions, riblets can delay the development of turbulent structures in the transitional zones during bypass transition, shifting the point of transition downstream. The asymptotic analysis carried out in [42] also indicates that riblets exert a destabilizing action on the evolution of Tollmien-Schlichting waves in a laminar flow but stabilize the longitudinal vortices that might be involved in bypass transition. Since bypass transition is observed in many practical applications, studying the development of secondary instabilities in the flow over riblets can have a strong possible impact on drag reduction through transition delay.

The primary objective of this work is thus to investigate modal and nonmodal stability analysis of the flow over a rough surface. Since we consider the laminar flow over the riblets, the focus is on the laminar-turbulent transition of the flow over such rough wall, with possible implications in the field of transition delay. The presence of a spanwise shear in the base flow velocity in the

presence of riblets suggests that the instability mechanism which initiates transition over the riblets may be different from that of the smooth wall. This is one of the many crucial issues that need further investigation if riblets are to be considered in industry applications [43]. To this purpose, a method based on the Bloch wave formalism [44] is proposed and applied on a channel flow with the bottom wall covered with streamwise independent trapezoidal riblets. Using this method, the modal instabilities found in the works of Moradi and Floryan [20] and Mohammadi *et al.* [23] are retrieved for validation. Moreover, the influence of the riblets on the lift-up mechanism and the development of streaks is investigated. Three regimes can be observed: for small spacings s, riblets slightly affect the transient energy amplification when detuned perturbations are considered, whereas fundamental (small wavelength) disturbances are strongly dampened. For $\pi/4 \leqslant s \leqslant \pi$, resonances leading to an increase of transient growth can be observed, at first for detuned instabilities only, and then, as s increases, also for fundamental ones. Ultimately, large spacings are associated with a more rapid (although slightly weaker) lift-up mechanism. In this case, the system does not select a unique ground state, which is a condition associated with geometric frustration [45]. Finally, resolvent analysis shows that the presence of riblets unexpectedly leads to the development of oblique waves, which may cause a quick transition to turbulence through nonlinear effects.

The remainder of the paper is structured as follows. Section II describes the flow over the riblets together with the governing equations. Section III introduces the linear stability problem. The computational framework is introduced in Sec. IV, with special care given in Sec. IV B to the method introduced in the work of Schmid *et al.* [39]. Section V presents the results obtained within the framework with Secs. V C and V D discussing, respectively, the transient growth and resolvent analyses. A summary of the main conclusions is provided in Sec. VI.

II. FLOW IN A CHANNEL WITH LONGITUDINAL RIBLETS

We consider the flow of an incompressible Newtonian fluid with viscosity ν^* in a channel of height $2h^*$ with the lower wall covered with riblets. The reference frame is chosen as $\mathbf{x}_0^* = (x_0^*, y_0^*, z_0^*)$, with x_0^*, y_0^*, and z_0^* being, respectively, the streamwise, wall-normal, and spanwise directions. The dynamics of the flow is governed by the Navier-Stokes equations:

$$\frac{\partial \mathbf{U}^*}{\partial t^*} = -(\mathbf{U}^* \cdot \boldsymbol{\nabla})\mathbf{U}^* - \frac{1}{\rho^*}\boldsymbol{\nabla} P^* + \nu^* \nabla^2 \mathbf{U}^*, \tag{1}$$

$$\boldsymbol{\nabla} \cdot \mathbf{U}^* = 0, \tag{2}$$

where the superscript asterisk indicates dimensional variables, $\mathbf{U}^* = (U^*, V^*, W^*)^T$ is the velocity field, and P^* is the pressure. No-slip boundary conditions are applied at the walls. The top wall is assumed to be smooth while streamwise invariant riblets are mounted on the bottom wall. The roughnesses are characterized by their peak height ϵ, the riblet spacing $s = 2a^*/h^*$, and their shape $\eta^*(z_0^*)$ (explicitly given in the Appendix). In most of the cases considered in this study, trapezoidal streamwise invariant riblets with a fixed height $\epsilon^* = 0.15h^*$ will be considered. The choice of this shape is not arbitrary: in the case of a channel with two rough walls, Moradi and Floryan [20] showed that these grooves represent an optimal choice for laminar drag reduction when both height and depth are imposed and kept equal.

The flow is characterized by the presence of two separate length scales: in the wall-normal direction y_0^*, the natural length scale is the half height of the channel h^* (taken between the center of the channel and the tip of the riblets) while, for the spanwise direction z_0^*, it is taken to be the spacing s of the riblets. Following Philip [46] and Picella *et al.* [47], we introduce the reference velocity $U_r^* = 3U_a^*/2$, with U_a^* being the average of the base flow velocity $U_a^* = 1/(2h^*)\int_{-h^*}^{+h^*} U^*(y^*)dy^*$ of the reference case of the channel flow without any riblets, which is one-dimensional. The most common choice of the centerline streamwise velocity as reference velocity is unsuitable in this case as it is dependent on the geometry of the roughness. Whereas, with the present choice of $U_r^* = 3U_a^*/2$, the Reynolds number remains fixed at a constant flow rate. Notice that U_r corresponds

to the maximum velocity in the flow field in the laminar smooth-wall case, while in the riblets cases it does not represent any intrinsic property of the flow, so that it is chosen as the reference velocity mostly for comparison purposes. Thus, the Reynolds number is defined as $\mathrm{Re} = U_r^* h^*/\nu^*$. In the following, all the physical quantities without the superscript asterisk are scaled by the channel half-height h^* and by the reference velocity U_r^*.

For all the configurations studied, the flow rate Q is fixed constant, which leads to an evolution of the pressure gradient as a function of the height ε and the spacing s of the riblets [20]. This constraint states that the flow rates in the smooth and grooved channels are identical. In this context, the laminar stationary base flow $\mathbf{U}_0(\mathbf{x}_0) = [U(y_0, z_0), 0, 0]^T$ in the grooved channel is described by the x-momentum equation of the form

$$\frac{\partial^2 U_0}{\partial y_0^2} + \frac{1}{s^2}\frac{\partial^2 U_0}{\partial z_0^2} = \mathrm{Re}\frac{dP_0}{dx_0}, \tag{3}$$

together with no-slip boundary conditions at the walls, which, in the normalized physical domain, are imposed at $0 \leqslant z_0 \leqslant 1$ and $-1 + \eta(z_0) \leqslant y_0 \leqslant 1$. Periodic boundary conditions are imposed in the spanwise direction.

Irregular boundary conditions can be tackled either via a domain transformation method [21,48] or through an immersed boundary conditions method [20,49]. The latter remains limited to small amplitude riblets. Thus, a domain transform technique is employed and, following Ehrenstein [21] and Mohammadi *et al.* [23], we introduce a coordinate system $\mathbf{x}_1 = (x_1, y_1, z_1)$ such as

$$x_1 = x_0, \quad z_1 = z_0, \quad y_1 = (1-\gamma)y_0 + \gamma, \quad \text{with} \quad \gamma = \eta(z_0)/[\eta(z_0) - 2]. \tag{4}$$

By means of this domain transformation, the physical domain $\mathbf{x}_0$ is mapped into a smooth channel in the computational domain $\mathbf{x}_1$ where $0 \leqslant z_1 \leqslant 1$ and $-1 \leqslant y_1 \leqslant 1$. The relations between the derivative operators of the two domains are given in the Appendix. In this domain, the Stokes equation (3) becomes $\nabla_1^2 U = -2$ where ∇_1^2 is the Laplacian written in the coordinate system, as given in Appendix. Notice that the fact of having only one rough wall is essentially linked to the use of such a simple coordinate transformation. Although this choice does not correspond to a realistic configuration that might be used in an industrial application, we are aware of many works considering riblets on only one wall (see [10,21,38,41] among others). Thus, for the sake of numerical simplicity, we have chosen to consider only one rough wall, although the results are easily extendable to the case of two rough walls.

III. LINEAR STABILITY EQUATIONS

The flow is decomposed into the two-dimensional base flow $\mathbf{Q}_0 = (\mathbf{U}_0(y_1, z_1), P_0)^T$ and a small perturbation $\mathbf{q}_1 = (\mathbf{u}_1, p_1)^T = (u_1, v_1, w_1, p_1)^T$ such as $\mathbf{Q}(\mathbf{x}_1, t) = \mathbf{Q}_0(\mathbf{x}_1) + \mathbf{q}_1(\mathbf{x}_1, t)$. The Navier-Stokes equations are linearized around the two-dimensional base flow yielding the following system:

$$\frac{\partial u_1}{\partial t} + U_0\frac{\partial u_1}{\partial x_1} + v_1\frac{\partial U_0}{\partial y_1} + \frac{w_1}{s}\frac{\partial U_0}{\partial z_1} = -\frac{\partial p_1}{\partial x_1} + \frac{1}{\mathrm{Re}}\nabla_1^2 u_1, \tag{5}$$

$$\frac{\partial v_1}{\partial t} + U_0\frac{\partial v_1}{\partial x_1} = -\frac{\partial p_1}{\partial y_1} + \frac{1}{\mathrm{Re}}\nabla_1^2 v_1, \tag{6}$$

$$\frac{\partial w_1}{\partial t} + U_0\frac{\partial w_1}{\partial x_1} = -\frac{1}{s}\frac{\partial p_1}{\partial z_1} + \frac{1}{\mathrm{Re}}\nabla_1^2 w_1, \tag{7}$$

$$\frac{\partial u_1}{\partial x_1} + \frac{\partial v_1}{\partial y_1} + \frac{1}{s}\frac{\partial w_1}{\partial z_1} = 0, \tag{8}$$

together with no-slip boundary conditions at the walls, i.e., $y_1 = \pm 1$ and $0 \leqslant z_1 \leqslant 1$, and periodic boundary conditions in the spanwise direction. Temporal stability is investigated considering

perturbations having the following modal expansion:

$$\mathbf{q}_1(x_1, y_1, z_1, t) = \tilde{\mathbf{q}}_1(y_1, z_1) \exp\left[i(\alpha x_1 - \omega t)\right] + \text{c.c.}, \tag{9}$$

where α is the real streamwise wavenumber, $\omega = \omega_r + i\omega_i$ the complex frequency of the wave, and $\tilde{\mathbf{q}}_1(y_1, z_1) = [\tilde{u}_1, \tilde{v}_1, \tilde{w}_1, \tilde{p}_1]^T$ is the associated eigenfunction. Ultimately, introducing the previous modal decomposition into Eqs. (5)–(8), the system takes the following form:

$$-i\omega\tilde{u_1} + i\alpha U_0\tilde{u_1} + \tilde{v_1}\frac{\partial U_0}{\partial y_1} + \frac{\tilde{w_1}}{s}\frac{\partial U_0}{\partial z_1} = -i\alpha\tilde{p_1} + \frac{1}{\mathrm{Re}}\nabla_1^2\tilde{u_1}, \tag{10}$$

$$-i\omega\tilde{v_1} + i\alpha U_0\tilde{v_1} = -\frac{\partial\tilde{p_1}}{\partial y_1} + \frac{1}{\mathrm{Re}}\nabla_1^2\tilde{v_1}, \tag{11}$$

$$-i\omega\tilde{w_1} + i\alpha U_0\tilde{w_1} = -\frac{1}{s}\frac{\partial\tilde{p_1}}{\partial z_1} + \frac{1}{\mathrm{Re}}\nabla_1^2\tilde{w_1}, \tag{12}$$

$$i\alpha\tilde{u_1} + \frac{\partial\tilde{v_1}}{\partial y_1} + \frac{1}{s}\frac{\partial\tilde{w_1}}{\partial z_1} = 0, \tag{13}$$

together with no-slip boundary conditions. The derivative and Laplacian operators in the new coordinate system are defined in the Appendix. The system (10)–(13) can be recast in the following compact form:

$$i\omega\tilde{\mathbf{q}}_1 = \mathbf{A}\tilde{\mathbf{q}}_1, \tag{14}$$

where the Jacobian of the system $\mathbf{A}$ is introduced. Due to the bidimensionality of the base flow, the system (10)–(13) constitutes a two-dimensional local eigenvalue problem [50] with periodic coefficients in the spanwise direction z_1. Notice that it can be further reduced by considering normal velocity and vorticity as a new set of variables [51]. Squire's theorem is also likely to be invalidated due to the spanwise velocity gradients in the base flow. However, if the spanwise gradients remain small, as appears to be the case for riblets with small spacing s, the theorem should hold "qualitatively," as found by Moradi and Floryan [20]. In the case they considered, the most unstable disturbances were three-dimensional but arose from the continuous deformation of a purely two-dimensional Tollmien-Schlichting (TS) wave induced by the riblets.

IV. COMPUTATIONAL FRAMEWORK

A. Spectral methods

In order to be solved numerically, both the Stokes equation for the base flow and the linear stability system need to be properly discretized. Spectral collocation methods [52] are chosen, yielding high accuracy even for a limited number of points. These methods have already been used to study the flow over riblets within different computational frameworks [20,21] or for similar global stability problems in different configurations [53,54]. The wall-normal and spanwise directions, y_1, z_1, are respectively discretized using Chebyshev and Fourier grids, yielding derivative operators $\mathbf{d}_y$ and $\mathbf{d}_z$. In order to be solvable, the two-dimensional problem is then transformed into a one-dimensional problem through tensor product manipulations [52]. Derivative operators in the computational domain $\mathbf{x}_1$ can be computed as follows:

$$\mathbf{D}_y = \mathbf{d}_y \otimes \mathbf{I}_z, \quad \mathbf{D}_z = \mathbf{I}_y \otimes \mathbf{d}_z, \tag{15}$$

where $\mathbf{I}_y$ and $\mathbf{I}_z$ are respectively the identity matrices of size $N_y \times N_y$ and $N_z \times N_z$ and $\otimes$ is the Kronecker tensor product. Second-order derivatives and weight matrices can be obtained in a similar way.

B. Bloch wave formalism

Performing a linear stability analysis on a system composed of only one riblet would be of little interest, since coherent structures within the flow can span multiple spacings of the roughnesses.

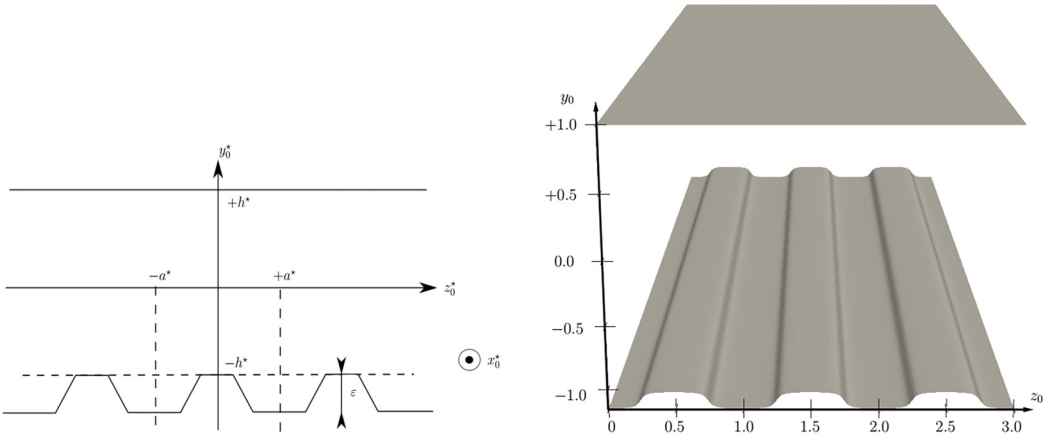

FIG. 1. Sketch of the channel and of the riblet geometry considered. The domain is normalized in the spanwise direction.

On the other hand, solving the two-dimensional problem for a large number of riblets would yield a prohibitive computational cost. Usually, linear stability of such a system is investigated via a spatial Floquet analysis [15,20,23], assuming that the roughness can be accurately described by a few leading Fourier modes.

Instead, we propose an alternative method which allows the computation of the solution (at a reasonable numerical cost) of the stability problem for a system composed of an arbitrary number n of riblets. It is based on the computational framework presented in the work of Schmid *et al.* [39]. For clarity, the method will be presented in the following. Consider a system consisting in the repetition of n riblets in the spanwise direction. The system can be decomposed and reordered into n smaller subsystems, each describing the flow into the subunit and its interactions with the adjacent subunits. In particular, since the base flow is periodic in spanwise direction z, $\mathbf{Q}_0(y_1, z_1) = \mathbf{Q}_0(x_1, y_1, z_1 + 2ka)$ (see Fig. 1), and the linearized dynamics of the complete system is governed by

$$\frac{\partial \mathbf{q}_1}{\partial t} = \mathbf{A}\mathbf{q}_1,$$

where the matrix $\mathbf{A}$ is a block-circulant matrix which is a particular case of the Toeplitz matrix. For the subsystem (j) the linearized dynamic can be written

$$\frac{\partial \mathbf{q}_1^{(j)}}{\partial t} = \mathbf{A}^{(j)}\mathbf{q}_1^{(j)},$$

where the disturbance state vector in the jth subunit is denoted as $\mathbf{q}_1^{(j)}$, and $\mathbf{A}^{(j)}\mathbf{q}_1^{(j)} = \sum_k \mathbf{A}_k^{(j)}\mathbf{q}_1{}_k^{(j)}$. Thus, the whole system can be recast under the following form:

$$\frac{\partial}{\partial t}\begin{pmatrix} \mathbf{q}_1^{(0)} \\ \mathbf{q}_1^{(1)} \\ \vdots \\ \mathbf{q}_1^{(n-1)} \end{pmatrix} = \underbrace{\begin{pmatrix} \mathbf{A}^{(0)} & \mathbf{A}^{(1)} & \dots & \mathbf{A}^{(n-1)} \\ \mathbf{A}^{(n-1)} & \mathbf{A}^{(0)} & \dots & \mathbf{A}^{(n-2)} \\ \vdots & \vdots & & \vdots \\ \mathbf{A}^{(1)} & \mathbf{A}^{(2)} & \dots & \mathbf{A}^{(0)} \end{pmatrix}}_{\mathbf{A}} \underbrace{\begin{pmatrix} \mathbf{q}_1^{(0)} \\ \mathbf{q}_1^{(1)} \\ \vdots \\ \mathbf{q}_1^{(n-1)} \end{pmatrix}}_{\tilde{\mathbf{q}}_1}, \tag{16}$$

with $\mathbf{A}$ the Jacobian associated to the full stability problem. It is decomposed into the matrices $\mathbf{A}^{(0)}$ and $\mathbf{A}^{(j)}$ (for $j = 1, \dots, n-1$) describing, respectively, the dynamics in a subunit and the coupling

interactions between subunits. If we consider that a subunit can interact only with adjacent subunits (i.e., nearest-neighbour coupling), then the Jacobian $\mathbf{A}$ reduces to a block-tridiagonal matrix. Only the three-unit subgroup $(\mathbf{A}^{(0)}, \mathbf{A}^{(1)}, \mathbf{A}^{(n-1)})$ is nonzero, significantly reducing the complexity and computational cost of the method.

Note that the Jacobian matrix $\mathbf{A}$ is block circulant due to the specific n-periodic nature of the system and can become block diagonal through the similarity transformation:

$$\mathbf{P}^H \mathbf{A} \mathbf{P} = \mathrm{diag}(\hat{\mathbf{A}}^{(0)}, \hat{\mathbf{A}}^{(1)}, \ldots, \hat{\mathbf{A}}^{(n-1)}) \equiv \hat{\mathbf{A}}, \tag{17}$$

where the transfer matrix $\mathbf{P}$ can be found analytically as

$$\mathbf{P} = \mathbf{J} \otimes \mathbf{I} \tag{18}$$

with $\mathbf{J}$ a matrix such as $\mathbf{J}_{j+1,k+1} = \rho_j^k / \sqrt{n}$ for $j, k = 1, \ldots, n-1$ and $\rho_j = \exp(2i\pi j/n)$ the nth roots of unity. The symbol $\otimes$ denotes the usual Kronecker product and $\mathbf{I}$ the identity matrix. With this transformation, the linear stability problem has been reduced to the study of n smaller subsystems characterized by the matrices $\hat{\mathbf{A}}^{(j)}$. The eigenproblems associated with the matrices $\hat{\mathbf{A}}^{(j)}$ are solved with a Krylov-Schur algorithm coupled with a shift-and-invert method. Ultimately, the full spectrum of the matrix $\mathbf{A}$ can be found from the merging of the n spectra of $\hat{\mathbf{A}}^{(j)}$ for $j = 1, \ldots, n-1$. Similarly, provided $\mathbf{v}_j$ is an eigenvector of $\hat{\mathbf{A}}^{(j)}$, the eigenfunctions of the full system can be retrieved and take the form $[\mathbf{v}_j, \rho_j \mathbf{v}_j, \rho_j^2 \mathbf{v}_j, \ldots, \rho_j^{n-1} \mathbf{v}_j]^T$ for $j = 1, \ldots, n-1$.

The equivalence with the Floquet analysis and its detuning factor ϵ can be dicussed. After Fourier expanding the base flow, it can be found (see [20] for example) that the perturbation has the following modal expansion:

$$\mathbf{q}_2(x, y, z, t) = e^{i\omega t} e^{i\alpha x} \sum_m \hat{\mathbf{q}}_m(y) e^{i(m+\epsilon)\beta_0 z}. \tag{19}$$

Recalling that the system is n periodic, the detuning factor can only be a limited number of n discrete values such as $\epsilon_j = \pm j/n, \;\; j = 1, \ldots, n/2$. Reintroducing this expression of the detuning factor into the Floquet modal expansion yields for $j = 1, \ldots, N-1$,

$$\mathbf{q}_2^j(x, y, z, t) = e^{i\omega t} e^{i\alpha x} e^{ij(\beta_0/n)z} \sum_m \hat{\mathbf{q}}_m(y) e^{im\beta_0 z} \tag{20}$$

$$= e^{i\omega t} e^{i\alpha x} e^{ij(\beta_0/n)z} \tilde{\mathbf{q}}(y, z) \tag{21}$$

$$= e^{ik_j z} \tilde{\mathbf{q}}_2(x, y, z, t), \tag{22}$$

where $k_j = \epsilon_j \beta_0 = j\beta_0/n$ is the Bloch wavenumber and $\tilde{\mathbf{q}}_2(x, y, z, t)$ is a $2\pi/\beta_0$-periodic function. Thus, the Bloch theorem for the system with the n subunits is retrieved.

Most importantly, transient growth and resolvent analyses [24] can also be realized within the same framework. Introducing a harmonic forcing of the form $\mathbf{f}_1 = \hat{\mathbf{f}}_1 e^{i\Omega t}$, the system (14) takes the following form:

$$\frac{\partial \mathbf{q}_1}{\partial t} = \mathbf{A}\mathbf{q}_1 + \mathbf{f}_1. \tag{23}$$

In the case in which the system is not harmonically forced (i.e., when $\mathbf{f}_1 = 0$), it is interesting to identify the perturbation to the base flow, $\mathbf{u}_1(0)$, able to provide at a given target time T the maximum energy amplification defined as

$$G(t) = \max_{\mathbf{u}_1(0)} \frac{E[\mathbf{u}_1(t)]}{E[\mathbf{u}_1(0)]} = ||\exp(\mathbf{A}t)||_E^2, \tag{24}$$

where $E[\mathbf{u}_1(t)] = ||\mathbf{u}_1||_E = \int_V |\mathbf{u}_1^2| dV$ is the kinetic energy of the perturbation, whereas, in the case in which the presence of a harmonic forcing is considered (i.e., $\mathbf{f}_1 \neq 0$) an optimal response to the

forcing can be defined as

$$H(\Omega) = \max_{\mathbf{f}_1} \frac{E(\mathbf{u}_1)}{E(\mathbf{f}_1)} = ||(i\Omega\mathbf{I} - \mathbf{A})^{-1}||_E^2. \tag{25}$$

Here we have used the energy for evaluating the growth of perturbation, although other quantities of interest might be considered as well. Numerically, the norm is defined through the imposition of a weight matrix $\mathbf{Q}_0$, identical for each subsystem. Besides the amplification curves, the "optimal" perturbation $\mathbf{u}_{\text{opt}}$ and forcing $\mathbf{f}_{\text{opt}}$ yielding, respectively, the maximum energy growth and maximum response at a target time T can be obtained [25,44]. These disturbances can be retrieved through a singular value decomposition [39,44] defined as follows:

$$\mathbf{U}_j \Sigma_j \mathbf{V}_j^H = \text{SVD}\left[\mathbf{F}_0 f(\hat{\mathbf{A}}_j)\mathbf{F}_0^{-1}\right], \tag{26}$$

where f is defined as $f(\mathbf{A}) = \exp(\mathbf{A}t)$ for the optimal perturbation and as $f(\mathbf{A}) = (i\Omega\mathbf{I} - \mathbf{A})^{-1}$ for the optimal forcing. As for the linear stability eigenfunctions, principal left and right singular vectors, representing optimal perturbation (or forcing depending on f) at initial and target times, take the following form:

$$\mathbf{u}_{\text{opt}}(0) = \begin{pmatrix} \mathbf{u}_j \\ \rho_j \mathbf{u}_j \\ \rho_j^2 \mathbf{u}_j \\ \vdots \\ \rho_j^{n-1} \mathbf{u}_j \end{pmatrix}, \quad \mathbf{v}_{\text{opt}}^H(T) = \begin{pmatrix} \mathbf{v}_j^H \\ \rho_j \mathbf{v}_j^H \\ \rho_j^2 \mathbf{v}_j^H \\ \vdots \\ \rho_j^{n-1} \mathbf{v}_j^H, \end{pmatrix} \tag{27}$$

where ρ_j is the root of unity yielding the largest singular value. As for the linear stability analysis, optimal perturbations and forcings can be now obtained for the whole system by calculating the singular value decomposition associated with the n smaller subsystems.

V. RESULTS

A. Laminar base flow

The presence of riblets on the channel walls induces variations of the shear-stress distribution in their neighborhood, yielding changes in the drag generated at the wall. These changes can be quantified by comparing the pressure gradients required to obtain the same flow rate in a rough channel and in a smooth channel of equivalent height. Mathematically, introducing the pressure gradients ΔP_s and ΔP_r, respectively corresponding to smooth and rough walls, the correction of the pressure gradient is simply expressed as $\delta P = \Delta P_r - \Delta P_s$. The evolution of this quantity as a function of the roughness height ϵ and spacing s is displayed in Fig. 2. For $s \geqslant 6$, the pressure correction is positive indicating a drag reduction effect, whereas for $s < 6$ the expected drag reduction effect is observed. For comparison, in the case of a wavy rough wall, the critical spacing was found to be $s \approx 3.65$ [20]. This drag-reduction effect can be explained as a consequence of the change of the base flow topology, which can be seen in Fig. 3. In the case of small s, the flow is lifted above the tip of the riblets due to viscous friction. The region of stagnation in the grooves leads to the formation of a strong spanwise shear in the velocity profile, potentially responsible for a destabilization of the flow [44]. For larger s, the presence of the riblets modulates the local centerline velocity, thus generating strong spanwise velocity gradients at the center of the channel. In both cases, the instability mechanisms may lead to Kelvin-Helmholtz related instabilities.

In the remainder of this study, riblets with a fixed height $\epsilon = 0.15$ and spacing $0.25 < s < 4.5$ will be considered, for which the pressure correction is negative and thus a drag reduction effect is observed. As stated by [20], at fixed riblets height (as in the present case) the lower bound on the pressure gradient correction due to the presence of riblets can be determined by ignoring the

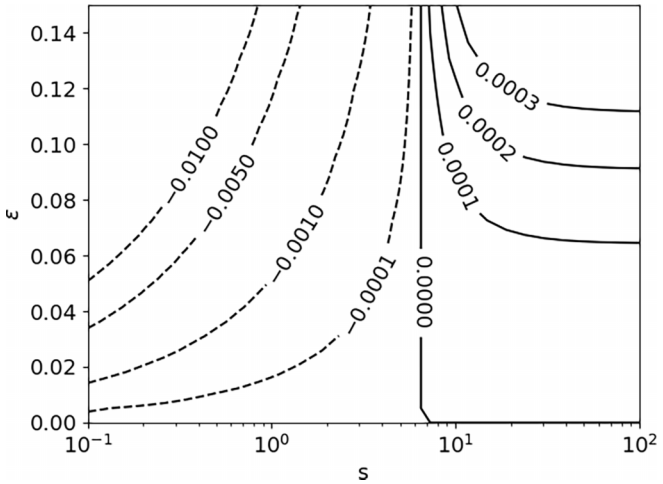

FIG. 2. Variations of the pressure gradient correction δP as a function of the spacing s and height ϵ.

boundary layer and approximating with the flow in a channel with the height reduced by the riblets height ϵ, i.e., $\mathrm{Re}\partial p_0/\partial x = 2[1-(1-\epsilon/2)^{-3}]$. The above relation provides a good approximation of the pressure gradient correction that riblets provide with respect to a smooth wall channel flow for sufficiently small riblets spacing, indicating that the change of pressure gradient in the cases considered here is indeed small.

B. Modal stability analysis

In a smooth channel, it is well known that two-dimensional TS waves with wavenumber $\alpha = 1.02$ become asymptotically unstable for $\mathrm{Re}_c \geqslant 5772$ [55]. This instability can be subcritically triggered even at Reynolds numbers as low as $\mathrm{Re}_c \approx 2700$ in the case of noisy environments. It has been experimentally shown [56,57] that the classical TS transition scenario is modified in the presence of surface roughness. Specifically, Moradi and Floryan [20] found that grooves with large spacing tend to stabilize the flow while small-wavelength riblets destabilize it. TS-like waves, modulated in the spanwise direction by the riblets were found to be the primary source of instability. However, in the case of riblets with large spacing, Mohammadi *et al.* [23] uncovered a new family of unstable

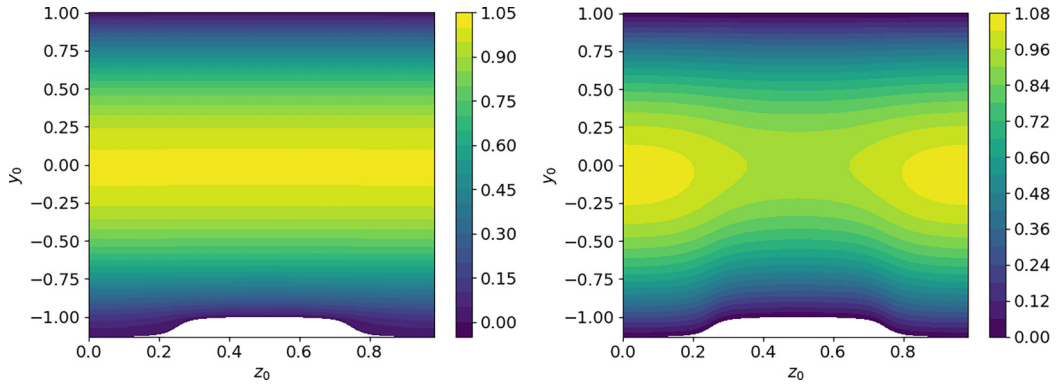

FIG. 3. Streamwise velocity component U of the base flow for the trapezoidal roughness and for $s = 0.25$ (left) and $s = 4.5$ (right), illustrating the two types of base flows.

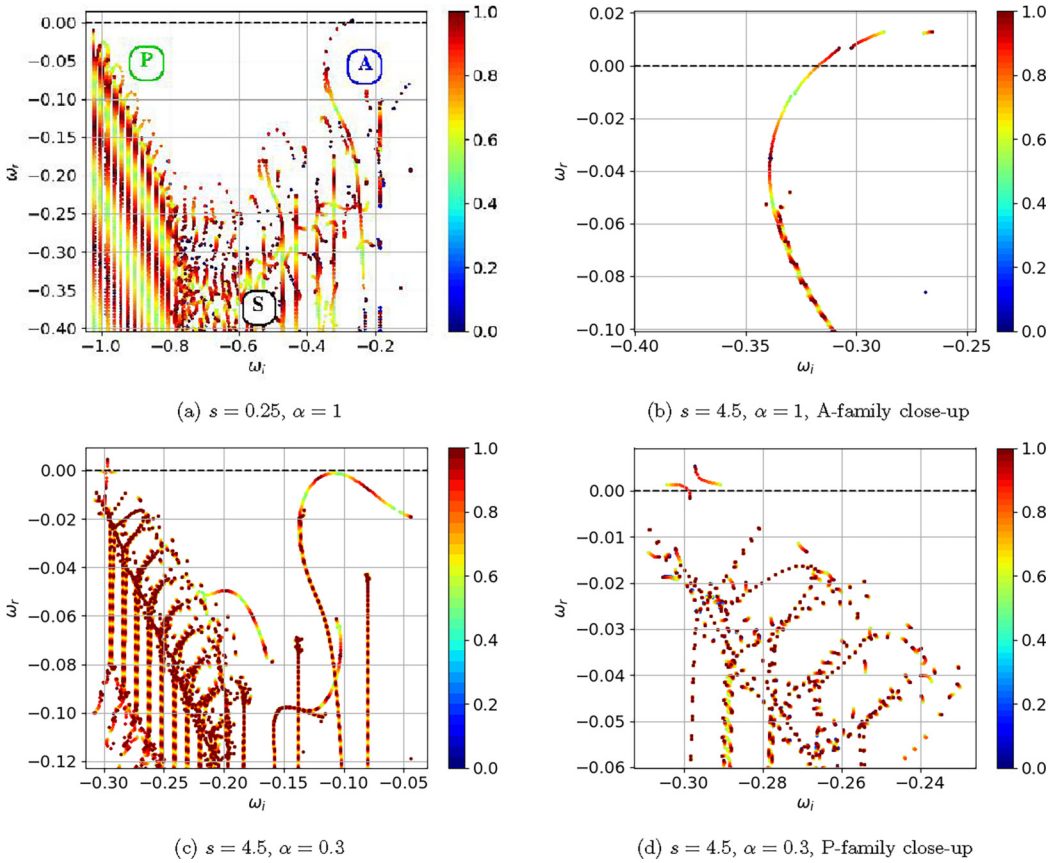

(a) $s = 0.25$, $\alpha = 1$

(b) $s = 4.5$, $\alpha = 1$, A-family close-up

(c) $s = 4.5$, $\alpha = 0.3$

(d) $s = 4.5$, $\alpha = 0.3$, P-family close-up

FIG. 4. Spectrum for the full system composed of $n = 50$ trapezoidal riblets for $\mathrm{Re} = 5000$ and different configurations of interest: $s = 0.25$ and $\alpha = 1$ for the spectrum in (a) and the close-up in (b); $s = 4.5$ and $\alpha = 0.3$ for the spectrum in (c) and the close-up in (d). The eigenvalues are colored according to the normalized phase $\theta_j = \arg(\rho_j)/2\pi$ of their respective root of unity ρ_j, whose value is reported in the legend. The detuned instabilities are those with the "brightest" colors (yellow/light blue). Red and black are for fundamental ones and green is for subharmonic.

modes associated with small streamwise wavenumbers, with a critical Reynolds number sensibly smaller than the one obtained from the TS instability. This mode was linked to an inviscid Kelvin-Helmholtz-like instability caused by the spanwise modulation of the base flow velocity in the center of the channel.

In this work, linear stability analysis is investigated for a system composed of $n = 50$ riblets, assuming nearest-neighbor coupling. In Jouin *et al.* [58] it has been demonstrated, for a very similar flow system (i.e., the secondary instability of crossflow vortces in a boundary layer) that dropping the hypothesis of nearest-neighbor coupling, and using $N_u = n$ instead of $N_u = 3$ coupled units (where n is the number of subunits) does not introduce any difference in the results. We are thus confident that using this assumption does not induce strong differences in the results, while allowing one to strongly reduce the computational cost of the stability analysis.

The eigenvalues spectra obtained for some notable cases are displayed in Fig. 4. The plots show the temporal frequency of the instability modes on the abscissa, and the associated growth rate on the ordinates. In case the dynamics remains laminar, the frequency and growth rate of the most unstable modes might be observed in a temporal signal taken from a probe, at least in the presence of a very

low turbulence/noise level to ensure a modal transition to turbulence. Notice that each spectrum, obtained for a given value of s and α specified in the subcaptions, is composed of the merging of $n = 50$ subspectra, obtained by solving the eigenvalue problems associated with the matrices $\hat{\mathbf{A}}^{(j)}$. Eventually, for systems with a sufficiently large number n of subsystems, the spatial branches can be entirely reconstituted. The eigenvalues are colored according to the normalized phase $\theta_j = \arg(\rho_j)/2\pi = j/n$ of their respective root of unity (see legend within the figures). Note that only half of the eigenvalues are visible as the eigenproblems associated with ρ_j and ρ_{n-j} share the same eigenvalues. This degeneracy of the eigenvalues stems from a symmetry of the three subunit group: the coupling between the left and center is identical to the one between the right and center subunits [24]. Following the secondary instability framework [59], the instability is said to be fundamental if $\theta = 0$ or $\theta = 1$, in the sense that it shares the same spatial spacing as the original. Similarly, instabilities with $\theta = 1/2$ (that is twice the initial spatial wavelength) and $0 < \theta < 1/2$ (arbitrary wavelengths) are respectively said to be subharmonic and detuned.

The spectra displayed in Fig. 4 are obtained for $\mathrm{Re} = 5000$ and $\epsilon = 0.15$ but for two different configurations, corresponding to the two types of instability of the flow over rough surfaces. The top-left spectrum is computed for $\alpha = 1$ and $s = 0.25$ and exhibits a structure similar to the one found for a two-dimensional Poiseuille flow. It is composed of three main parts, typical of the plane Poiseuille flow, originally denoted by Mack [60] as (i) the A branch, characterized by wall modes such as TS waves, (ii) the P branch, composed of Squire modes located in the center of the channel and usually stable, and (iii) the S branch which represents the continuous part of the spectrum [61]. In the present study, the term "branch" in these expressions will be replaced by the word "family" while the word branch will be used to denote the ensemble of eigenmodes resulting from the variation of the root of unity. Note that in this configuration, a smooth Poiseuille flow of equivalent height is stable, indicating the destabilizing effect of the riblets as already found in numerous studies [20,21,23].

For larger spacings and the same value of α, as shown in the top-right frame of Fig. 4, the instability still arises from the TS branch. However, in this case, it appears divided into three sub-branches [see the close-up in Fig. 4(b)], two of them being fully unstable while the other only partially. The breaking of the continuity of the TS branch denotes a topological change of the spectrum and a shift in the nature of the eigenmodes constituting the sub-branches. The maximum growth rate, $\omega_r = 0.016$, is reached by two modes located on the tip of these branches. Interestingly, one of the modes is subharmonic while the other is fundamental. If the height ϵ of the roughness is reduced, the three sub-branches merge together and the most unstable mode reconnects with the classic two-dimensional TS mode.

The spectrum obtained with $s = 4.5$ and $\alpha = 0.3$ is displayed in Fig. 4(c). Several observations can be made: the instability now arises from center Squire modes pertaining to the P family. This is the instability mode that was discovered and investigated in the work of Mohammadi *et al.* [23]. To be accurate, the instability stems from two unstable branches: the most unstable one reaches its maximum growth rate, $\omega_r = 0.005$, for ρ_0, underlining the fundamental nature of the instability. On the contrary, for the second branch, the maximum growth rate, $\omega_r = 0.0013$, is obtained with a desynchronized mode (ρ_{12}). Also note that the P family now looks like a succession of small Poiseuille flow spectra. For small streamwise wavenumbers, the TS branch is now marginally stable with its most unstable mode being subharmonic.

Figure 5(a) depicts a three-dimensional view of the streamwise velocity component of the most unstable mode found for $\mathrm{Re} = 5000$, $s = 0.25$, and $\alpha = 1$. The most unstable mode is reminiscent of the usual two-dimensional TS wave. In fact, the eigenfunction directly stems from the continuous deformation of a TS wave induced by the riblets, which loses its spanwise modulation when the roughness height ϵ tends towards 0. The modulation induced by the presence of the riblets, leads to the formation of strong spanwise and wall-normal shears. Depending on the strength of the spanwise velocity gradient, the flow is likely to be further destabilized by secondary Kelvin-Helmholtz-like instabilities. The concentration of momentum at the tip of the roughness has been identified by [8,14] as a necessary condition for the development of spanwise independent structures called

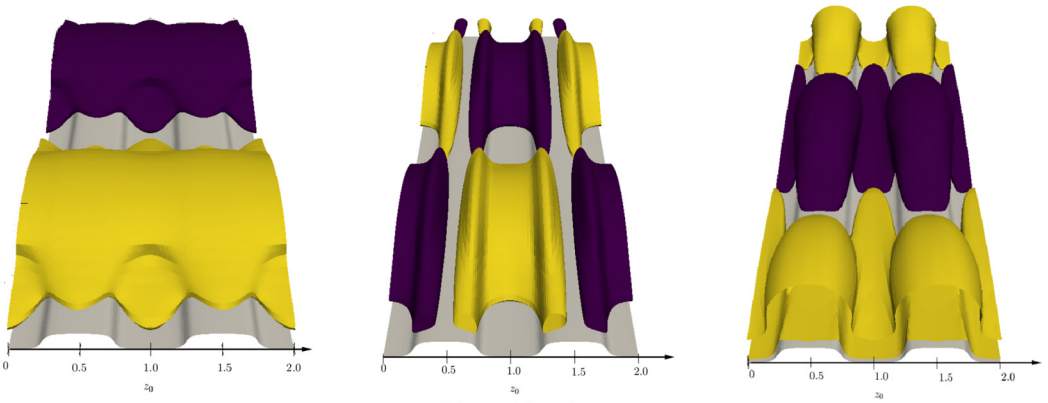

(a) $s = 0.25$ and ρ_0 (b) $s = 4.5$ and ρ_{25} (c) $s = 4.5$ and ρ_0

FIG. 5. Three-dimensional representation of the streamwise velocity perturbation of the most unstable fundamental mode for $\mathrm{Re} = 5000$, $\alpha = 1$, and for different configurations. Isosurfaces are taken as $u = \pm 0.75 u_{\max}$. Only half the channel is displayed for visibility.

Kelvin-Helmholtz rollers. These structures are linked to a Kelvin-Helmholtz-like instability and, despite having been originally identified in turbulent flows, may also emerge in transitional flows. The roughness also causes the appearance of a spanwise velocity component near the tip of the riblets. Despite being small, it could still play a significant role in supercritical transition scenarios where transition happens through three-dimensionalization of the flow via secondary instabilities of the TS wave [59].

Two of the unstable modes found for the same value of the streamwise wavenumber, but for larger spacings (i.e., $s = 4.5$) are shown in Figs. 5(b) and 5(c). The fundamental mode, provided in Fig. 5(c), bears some resemblance to the TS-like unstable mode observed for smaller spacings, although it appears more deformed than the former, whereas, the desyncronized mode provided in Fig. 5(b) presents not only a streamwise but also a spanwise alternation of low- and high-streamwise velocity perturbations, having the same spacing of the roughness, and mostly localized on the flanks of the roughness elements. This mode thus appears directly related to the geometry of the roughness, differently from the previously discussed ones, which arise as a deformation of two-dimensional TS modes.

Finally, for $s = 4.5$ and $\alpha = 0.3$, the most unstable center modes of the two branches are shown in Fig. 6. Streamwise and spanwise velocities are one order of magnitude higher than the wall-normal component and share the same shape: counter-rotating rolls oriented across the channel and propagating in the streamwise direction. In the fundamental case, rolls are centered at the widest channel opening while they are placed in a staggered pattern for the ρ_{12} mode. The staggered mode spans approximately four riblets. In both cases, instability arises from the modulation of the centerline velocity which induces strong spanwise velocity gradients in the middle of the channel, which may destabilize the flow through different mechanisms.

C. Transient growth analysis

Transient growth plays a fundamental role in the generation of streaks that lead to bypass transition to turbulence and that sustain it [27,28,30,62]. In turbulent flows, the presence of riblets weakens the lift-up mechanism that generates streaky structures, since the cross-flow motion, necessary for the formation of the counter-rotating vortices, faces a greater resistance. In turn, the generated vortices are weaker than in a smooth channel flow and are located further away from the channel, eventually limiting the possibility of momentum transfer towards the streamwise velocity

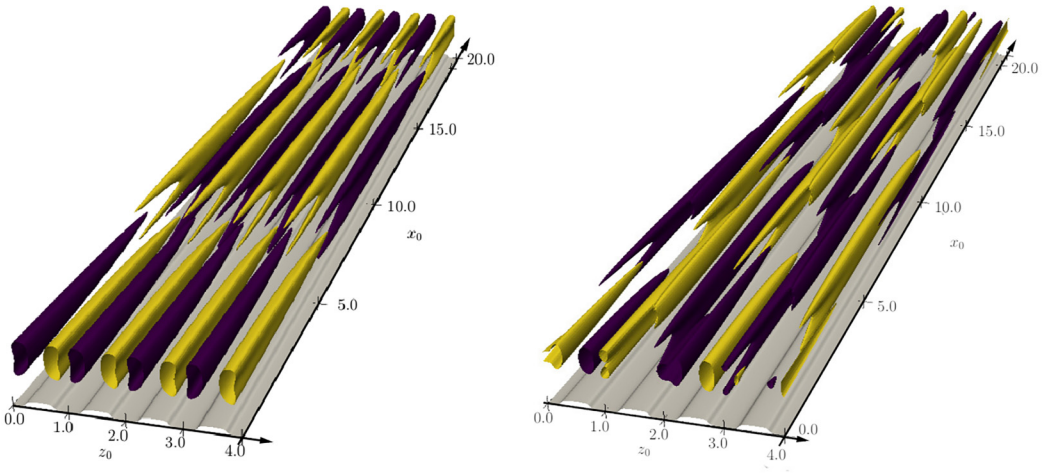

FIG. 6. Three-dimensional representation of the streamwise velocity perturbation for $s = 4.5$, $\mathrm{Re} = 5000$, and $\alpha = 0.3$ corresponding to center modes. Left: fundamental mode with complex frequency $\omega = 0.0053 - 0.2971i$. Right: detuned mode with complex frequency $\omega = 0.0013 - 0.3020i$.

component of the flow [6,12]. Although the effect of riblets on turbulent shear flows is by now well known, it is still unclear how they affect transient growth in laminar flows.

Figure 7 displays the gain G as a function of time for $\mathrm{Re} = 5000$, $\alpha = 0$, and different spacings s. As per the eigenvalues, the amplification curves are colored according to their respective root of unity and only half of the curves are visible due to the coupling symmetry. In all cases, the maximum energy growth, reached for detuned modes, as well as the time at which this maximum is reached, remains close to the one found for a smooth channel flow. Only in the case of large spacing do the riblets appear to induce an acceleration in the transient growth mechanism as the optimal time goes from $T_{\mathrm{opt}} = 385$ to $T_{\mathrm{opt}} = 150$.

For small spacings [Figs. 7(a) and 7(b)], comparing the maximum transient growth obtained for detuned modes (colored curves) to that with ρ_0 (solid black curves), one can observe a difference of more than one order of magnitude. Notably, if the transient growth analysis would have been realized on a system composed of a single subunit, a much weaker optimal energy gain would have been obtained. In fact, in this configuration, the size of a single subunit is too small to account for a large-scale phenomenon such as the lift-up effect, underlining the necessity of considering a system spanning multiple subunits. The amplification curves also appear to display a scaling with respect to the fundamental spanwise wavenumber associated to the root of unity ρ_j, namely, $\beta_j = j\pi/ns$. In particular, the maximum gain scales as the square of β_j, in agreement with the scaling obtained by Gustavsson [64] for smooth channel flow. This is not too surprising: each amplification curve represents an optimal perturbation whose spatial spacing is governed by the corresponding root of unity.

For intermediate values of the riblet spacing, such as $s = \pi/4$ and $s = \pi$ [Figs. 7(b) and 7(c)], the energy amplification is significantly enhanced by the presence of the riblets, although in the former case this is true only for detuned modes (compare the dashed black line with the solid ones). This is likely a resonance effect as the riblet wavenumber is close to the spanwise wavenumber yielding the maximum optimal gain $\beta_{\mathrm{opt}} = \pi/s = 2$ in a smooth channel flow [44]. As the riblet spacing s is increased, the curves progressively superpose themselves. This phenomenon arises from a degeneracy of the largest singular value of the exponential propagator $\exp(\mathbf{A}t)$. However, this is not a trivial effect of the n-periodic symmetry. Mathematically, through the orthogonality of the Bloch modes, it can be demonstrated that the optimal perturbations are also orthogonal and thus form a

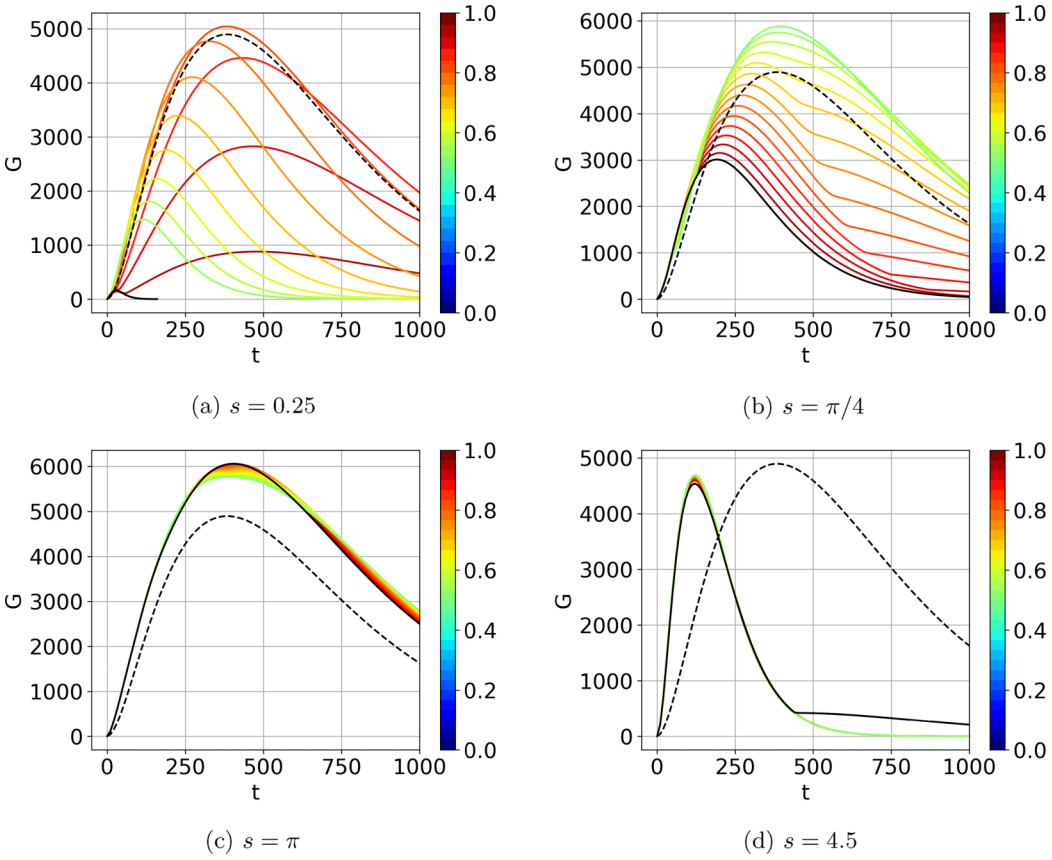

(a) $s = 0.25$ (b) $s = \pi/4$

(c) $s = \pi$ (d) $s = 4.5$

FIG. 7. Gain as a function of time for Re = 5000, $\alpha = 0$, and several riblet spacings. For clarity, the curve associated with ρ_0, corresponding to fundamental, spanwise invariant modes is denoted in black. Dotted line represents the amplification curve for a smooth channel at Re = 5000, $\alpha = 0$, and $\beta = 2$, which yields the maximum optimal gain for this configuration [63]. The other curves are colored according to the normalized phase $\theta_j = \arg(\rho_j)/2\pi$ of their respective root of unity ρ_j, whose value is reported in the legend. The detuned instabilities are those with the "brightest" colors (yellow/light blue). Red and black are for fundamental ones and green is for subharmonic.

basis of the eigenspace associated with the leading degenerate singular value. Physically, we now have n optimal perturbations corresponding to different roots of unity and with different wavelengths but sharing almost the same maximum gain $G_{\max}$ and optimal time T_{opt} and representing different possible and equally probable paths in phase space. We can also notice that the trend of the energy gain with respect to the riblets spacing is in contrast to that observed for turbulent channel flows (see, for instance, Chavarin and Luhar [10], in which the gain initially decreases linearly with increasing riblet size, and then increases). This suggests that, at least in the present configuration, riblets are not suitable for transition delay.

We are now focusing our attention on the form of the optimal perturbations, which can be seen in Fig. 8. Cross-flow dynamics of the optimal initial disturbances for Re = 5000, $\alpha = 0$, and several riblet spacing s are shown in Fig. 8. In all cases, the optimal perturbation(s) corresponds to counter-rotating vortices (CV) similar to the ones observed in a smooth channel flow [63] as well as to those observed in turbulent channel flow over riblets [10]. Streamwise velocity disturbance is one order of magnitude weaker than the cross-flow components and is not represented. For $s = 0.25$, the CV span approximately six riblets, giving a spanwise wavenumber equal to $\beta = 2.09$. This is

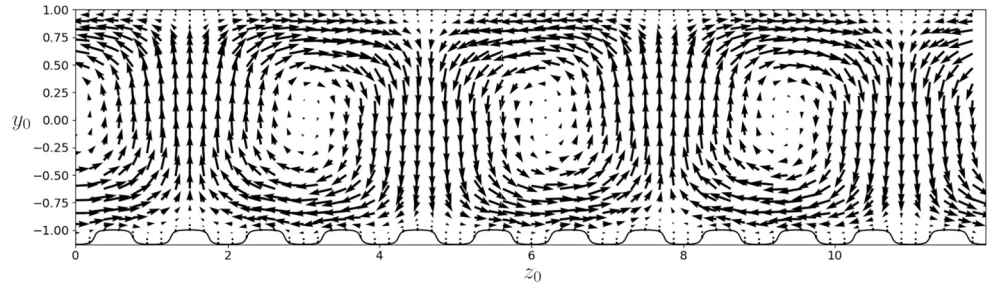

(a) $s = 0.25$

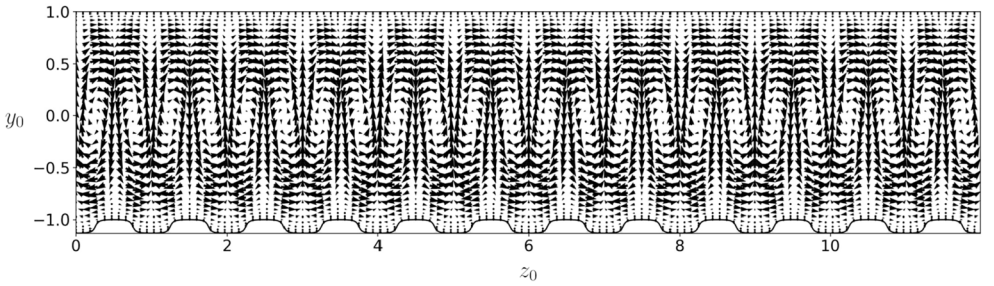

(b) $s = \pi/2$

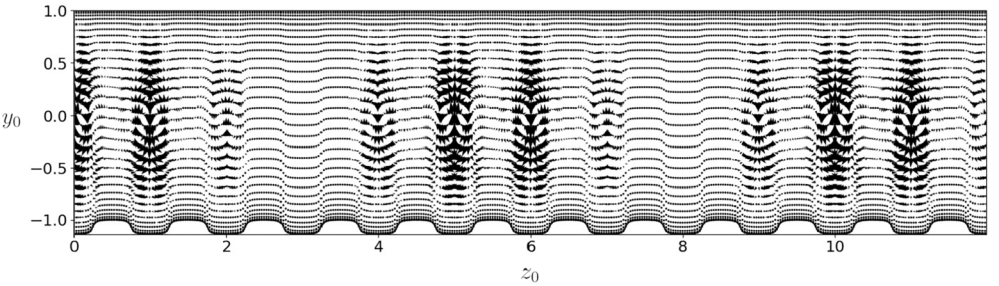

(c) $s = 4.5$

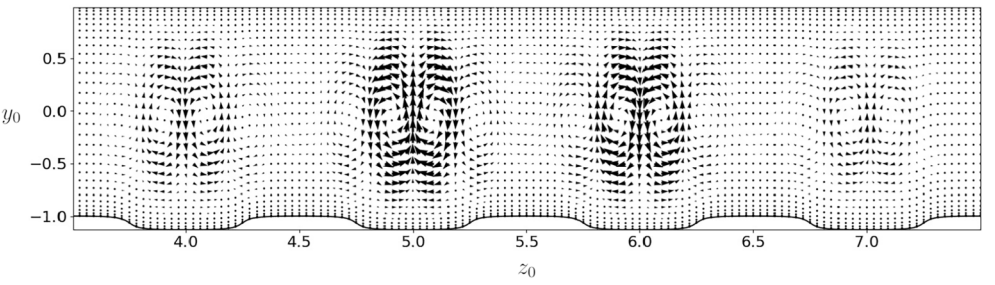

(d) $s = 4.5$, close-up of figure (c)

FIG. 8. Cross-flow dynamics ($v - w$ vectors) of the optimal perturbation at initial time for $\mathrm{Re} = 5000$ and $\alpha = 0$. For $s = 4.5$, the optimal perturbation associated with root of unity ρ_{12} has been arbitrarily chosen between the n possible choices. Streamwise velocity disturbance is one order of magnitude weaker than the cross-flow components and is not represented. The number of riblets visualized ($n = 12$) has been chosen for accommodating approximately two wavelengths of the counter-rotating optimal vortices for $s = 0.25$. Vectors are drawn every two points in the wall-normal direction and, in the spanwise direction, respectively, every nine, five, and two points for (a), (b), and (c).

quite close to the spanwise wavenumber yielding the maximum optimal gain $\beta_{\text{opt}} = 2$ in the smooth channel, indicating a limited influence of the riblets on the flow. If the riblet spacing is progressively increased, the wavelengths of the CV observed depart from the optimal value for the smooth channel and are closer to the riblets' own wavelength, indicating a progressive synchronization of the optimal perturbation wavelength with that of the roughness. A complete synchronization occurs for $s = \pi/2$ for which the CV exactly spans one riblet, and is observed in all the cases for which a fundamental mode is the most amplified.

The last case considered is obtained with $s = 4.5$. One optimal perturbation among the n possible is presented in Fig. 8(c), with a close-up in (d). CV are still visible; however, they appear localized in regions with the widest channel opening and span only a third of a subunit. The corresponding wavenumber is $\beta = 2.11$, again quite close to β_{opt}. Differently from the two previously discussed configurations, the amplitude of the CV now appears modulated in the spanwise direction as a consequence of a beating phenomenon triggered by the superposition of two waves with incommensurable spanwise wavelengths. The optimal perturbations associated with other roots of unity are characterized by a similar shape, although with a different distribution of the CV as the spatial wavelengths involved in this beating phenomenon are different.

The mechanism responsible for the energy amplification, commonly called the lift-up effect [62], will lead to the formation of streamwise-independent coherent structures also known as streaks. The streaks resulting from the development of the optimal disturbances presented in Fig. 8 can be seen in Fig. 9. Physically, the lift-up mechanism is characterized by a transfer from the cross-flow velocity components to the streamwise velocity component. The spanwise wavelength of the optimal perturbations at the initial time remains the same no matter the spacing of the riblets. It is also important to say that the coherent structures in the near-wall region tend to be almost universal for wall-bounded turbulent flows, while in transitional flows there is not such a universality. However, structures such as streaks arising through transient growth are indeed observed in all wall-bounded shear flows during bypass transition (see [25,65] for boundary layer, Couette, and channel flows, among others). Although in the channel flow the structures span the whole channel, almost identical streaky structures are found in the boundary layer (of course, limited to the region in which the shear is sufficiently high) as well as in the Couette flow, among many other shear flows. Thus, we think that the present results can be easily extended to other shear flows in the framework of bypass transition.

The nonmodal behavior of the considered flow is thus strongly affected by the spacing of the roughness. For small s, the riblets' influence on the shape of the optimal perturbations appears limited as the initial optimal CV are characterized by a wavelength almost corresponding to that of a smooth channel flow. The streaks are lifted above the riblets and the flow behaves as in a smooth channel of smaller height. Riblets appear to have an impact limited to the near-wall zone, extending approximately from the tip of the roughness to $y = -0.9$, and modifying the shape of the optimal perturbations only locally. A close-up of the region in the vicinity of the roughness for $s = 0.25$ is provided in Fig. 10 for the wall-normal and spanwise velocities at the initial time. In this region, velocities are smaller than in the bulk of the channel but still non-negligible (around 10% of the maximum velocity) and exhibit a rather complex shape as shown by the spatial Fourier spectrum provided in Fig. 10(d). This also sheds some light on one small shortcoming of the ROG formulation: the assumption that the roughness shape can be accurately described by only a few leading Fourier modes is usually verified either through the convergence of the growth rate of the most unstable mode [15,20] or of the maximum gain [10,36]. However, even when these quantities appear well converged, some regions of interest like the vicinity of the riblets may require a much larger number of modes to be accurately described. For intermediate spacings, the CVs appear more deformed and have a wavelength departing from that recovered in the smooth channel flow. These optimal disturbances result from a competition between the natural, optimal wavenumber of the streaks and the parametric forcing due to the riblet. Resonance can be observed when the riblet wavenumber is equal to the optimal streak wavenumber or one of its subharmonics, yielding large energy amplification.

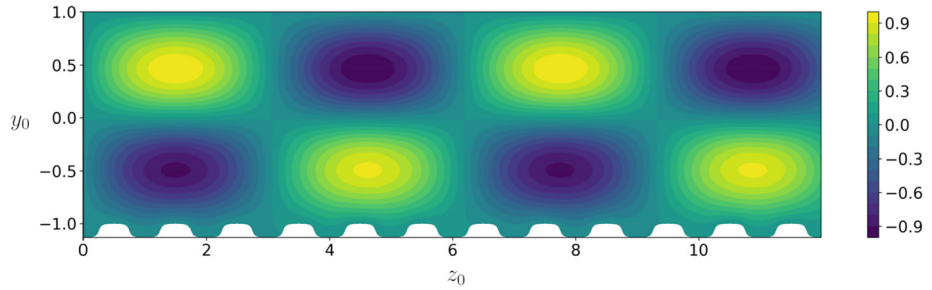

(a) $s = 0.25$

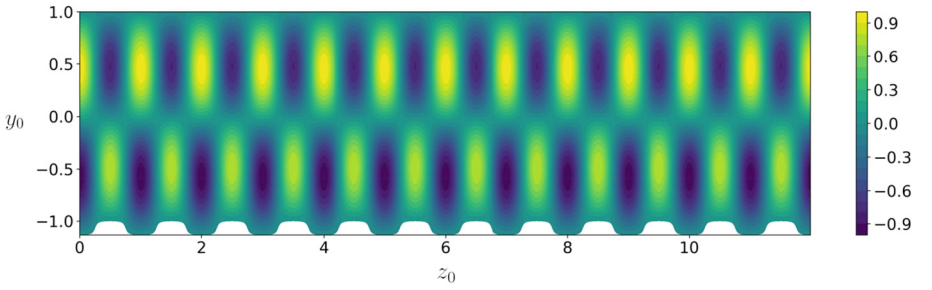

(b) $s = \pi/2$

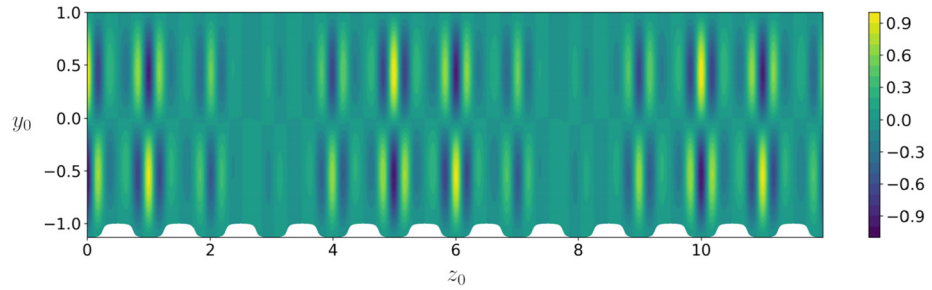

(c) $s = 4.5$

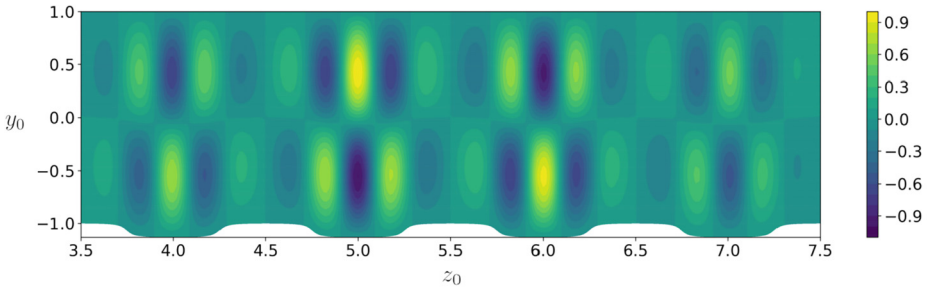

(d) $s = 4.5$, close-up of figure (c)

FIG. 9. Streamwise velocity component of the optimal perturbation at target time T_{opt} for $\text{Re} = 5000$, $\alpha = 1$, and different spacings s.

For large spacings, riblets constrain the streaks wavelength and n possible optimal perturbations could be found, having amplitude modulated in the spanwise direction. A similar mechanism has already been described for phase-locked lasers and is denoted as geometric frustration [45] (i.e., the inability of an ordered system to find a unique optimal state). The analogy with the present case appears quite clearly: competition arises between the lift-up mechanism generating CV and

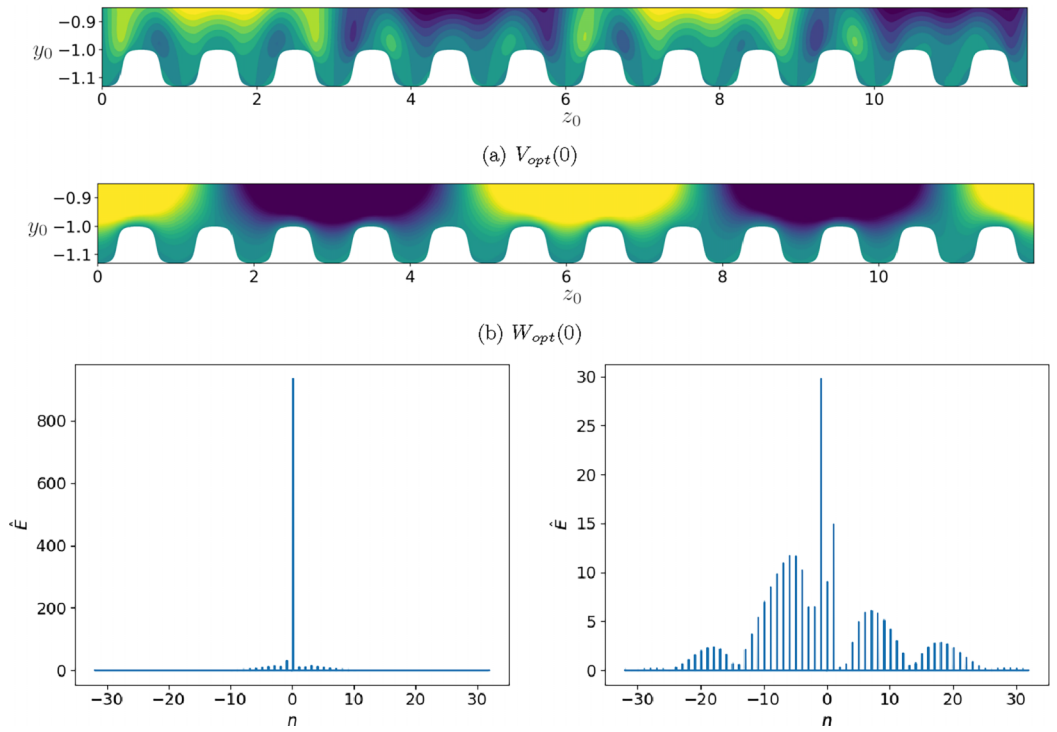

FIG. 10. Close-up in the near-riblet region of the cross-flow dynamics ($v - w$ vectors) of the optimal perturbation at initial time for Re $= 5000$, $\alpha = 0$, and $s = 0.25$. Streamwise velocity disturbance is one order of magnitude weaker than the cross-flow components and is not represented. The number of riblets visualized ($n = 12$) has been chosen for accommodating approximately two wavelengths of the counter-rotating optimal vortices. Bottom: spatial Fourier spectra of the wall-normal velocity disturbance taken at wall-normal positions $y = 0$ (left) and $y = -0.95$ (right).

streaks at an optimal wavenumber $\beta_{\text{opt}} \approx 2$ and the riblets, which act as a geometric forcing with wavenumber $\beta_f = \pi/s$. In the domain of fluid mechanics, a similar phenomenon was observed in the study of secondary flows in Rayleigh-Bénard convection with wavy walls [66]. More recently, the works of Hossain and Floryan [67,68] also showed the existence of a beating phenomenon in the secondary pattern and its link with a wavenumber lock-in phenomenon.

D. Resolvent analysis

A resolvent analysis allows the identification of high-energetic flow structures in both laminar and turbulent flows through a singular value decomposition of the forcing-response transfer function, commonly called the resolvent operator [24,69]. For a smooth channel flow, the response to a harmonic forcing is characterized by the presence of two pseudoresonances [44]: the strongest one leads to the generation of the most unstable TS wave while the other is linked to a center Squire mode.

Resolvent curves are displayed for Re $= 5000$, $\alpha = 1$, and different spacings in Fig. 11. In particular, the figures provide the evolution of the transfer function (the norm ratio of the response to the norm of the forcing) as a function of the frequency Ω of the forcing, for different riblet spacings s. The different colors of the curves indicate the root-of-unity value. The peaks in the transfer function $H(\Omega)$ correspond to quasiresonances. For smooth Poiseuille flow, it is well known that, for a nonzero value of the streamwise wave number α, there are two peaks, a first for $\Omega < 0.5$

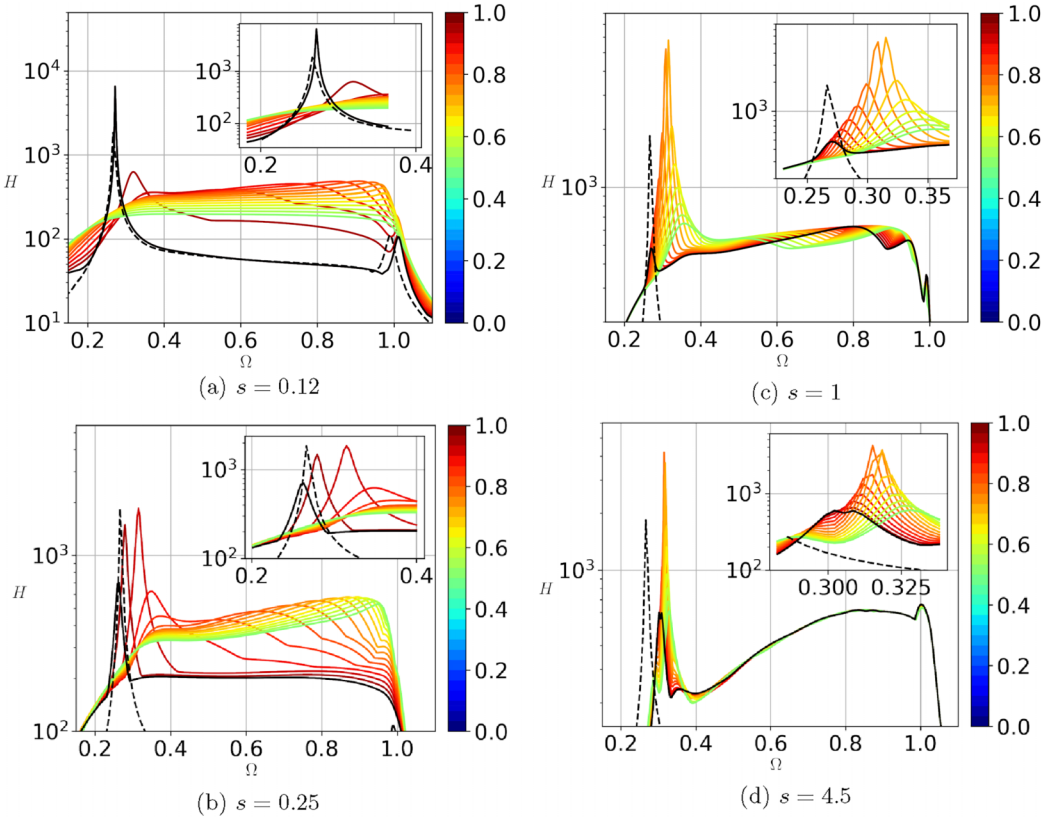

FIG. 11. Resolvent norm for Re = 5000, $\alpha = 1$, and different riblet spacings s. Dotted line represents the resolvent norm for a smooth channel flow with Re = 5000, $\alpha = 1$, and $\beta = 0$. The inset is a close-up on the first pseudoresonance. Black curve is the curve associated with ρ_0, corresponding to fundamental, spanwise invariant modes. The other curves are colored according to the normalized phase $\theta_j = \arg(\rho_j)/2\pi$ of their respective root of unity ρ_j, whose value is reported in the legend. The detuned instabilities are those with the "brightest" colors (yellow/light blue). Red and black are for fundamental ones and green is for subharmonic. The subplots represent a close-up of the quasiresonance regions of the resolvent norm.

corresponding to a quasiresonance with the A modes and a second for $\Omega \simeq 1$ corresponding to a quasiresonance with the P modes (see Schmid and Henningson [63]).

For small spacing $s = 0.12$, the two pseudoresonances found for the smooth channel flow are retrieved. The distinction between the two mechanisms is quite clear: only the fundamental mode experiences a pseudoresonance for $\omega = 0.27$ while the subharmonic and detuned forcings appear responsible for the excitation of the flow at larger frequencies. For these modes, the second pseudoresonance disappears and is replaced by a plateau formed by the superposition of several amplification curves associated with different roots of unity. In other words, as the frequency is increased, the optimal energy amplification of the whole system remains quasiconstant through an evolution of the forcings' spatial spacing. Despite yielding responses one order of magnitude below the pseudoresonance, these optimal forcings excite a very broad range of frequencies, making them relevant in a noise-triggered transition scenario (like the bypass transition) for which the probability to hit exactly the frequency of the pseudoresonance is small [70]. The mechanism associated with these forcings is known as the Orr mechanism [71]. It relies on the two-dimensional deformation of vortical structures by the mean flow. Structures which are initially aligned against the direction of the flow tend to realign themselves with it and, in doing so, generate transient growth through

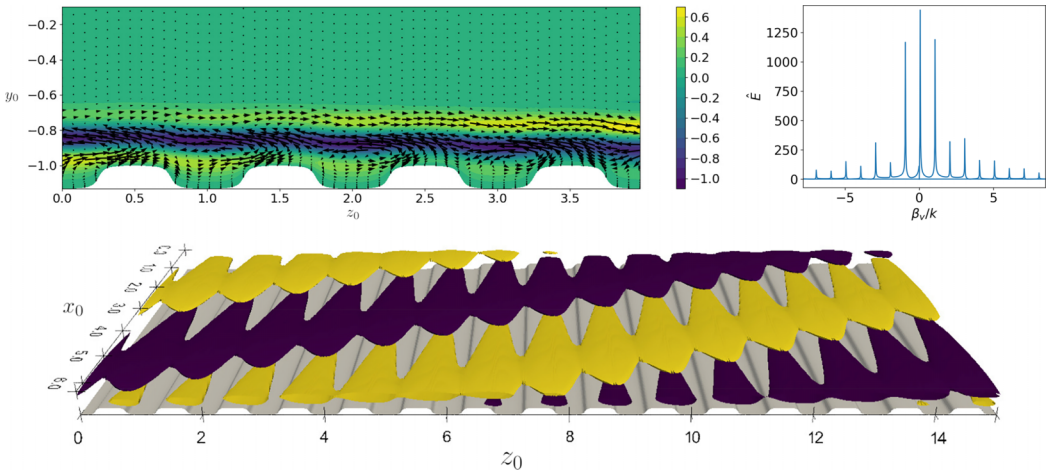

FIG. 12. Top left: optimal forcing for a system with Re $= 5000$, $\alpha = 1$, and $s = 0.25$. In the top frame, only four riblets are represented for the sake of visualization. The corresponding root of unity is ρ_2. The quiver plot depicts the cross-flow dynamics $(v - w)$. The contour plot depicts the streamwise velocity disturbance. For simplicity, only one side of the channel is being shown. Top right: Fourier transform in the spanwise direction of the optimal forcing. Bottom: optimal forcing for the same flow case. The isosurfaces of the streamwise velocity perturbation are shown.

the concentration of vorticity [72]. This result is a consequence of the energy optimization rather than a riblet-related effect, as is observed also for optimal perturbations in smooth channel flows. For larger wavelengths s, a few observations can be made. Most importantly, the riblets induce a desynchronization of the pseudoresonance: the maximum gain is now reached for a detuned mode (ρ_2 for $s = 0.25$), associated with a three-dimensional optimal forcing and response, as will be shown later. The detuning appears to increase as s is increased: maximum responses are obtained for ρ_8 ($s = 1$) and ρ_6 ($s = 4.5$). This three-dimensionalization is associated with a decrease of the maximum gain for small s before it returns to its original level or higher for intermediate and large s. A small shift in the pseudoresonance optimal frequency can also be seen as it goes from $\Omega_{\text{opt}} = 0.27$ to $\Omega_{\text{opt}} = 0.31$ for larger spacings. For $s = 4.5$, the amplification curves collapse, as previously observed in the transient growth analysis. Again, this superposition results from a degeneracy of the largest singular value of the resolvent operator which generates n equally amplified optimal forcing and responses. Physically, this also indicates the presence of a lock-in phenomenon for the forcings and their response in this range of frequency. In general, we can conclude that the riblet spacing s and the root of unity (i.e., the phase shift between the periodicity of the basic flow and the instability) strongly influence the form of the function of transfer $H(\Omega)$. In certain cases such as $s = 1$ or $s = 4.5$ the quasiresonance with the A modes is amplified while for $s = 0.25$ or $s = 0.12$ the quasiresonance of the A modes is attenuated in favor of a more broadband response.

We now turn our attention to the optimal forcing and responses corresponding to the first pseudoresonance. These are shown in Figs. 12–14 for increasing values of s. Notice that each optimal forcing is associated with a given temporal frequency Ω, so the velocity field, which should oscillate in time, is shown at an arbitrary phase. The velocity fields associated with the optimal forcings are three-dimensional and are characterized by strong streamwise and spanwise velocity components, while the wall-normal velocity component is one order of magnitude weaker. The optimal forcings appear as oblique waves with varying spatial wavelengths which eventually develop into deformed three-dimensional (3D) TS waves. With this in mind, it is important to remember that detuned modes with root of unity ρ_j do not exist by themselves but instead form a pair with the disturbance associated with the conjugate root of unity $\rho_j^* = \rho_{n-j}$. The desynchronization appears progressively: for small s the forcing couples 15 riblets and generates what resembles a 3D

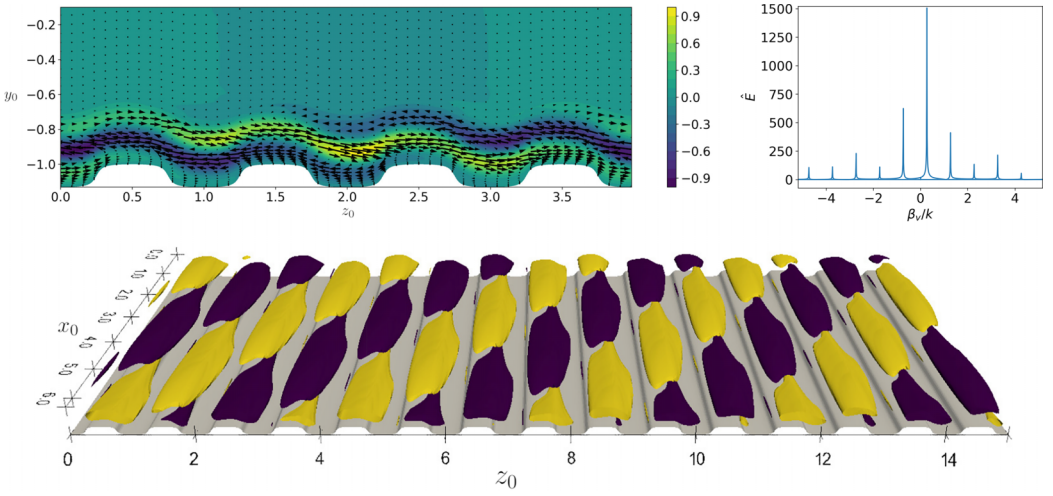

FIG. 13. Same as Fig. 12 for $s = 1$.

TS wave (see Fig. 12). Structures similar to the small vortices in the top corners of the riblets were also observed numerically by Goldstein and Tuan [13]. The streamwise component of the response, shown in a three-dimensional view in the bottom frames of the figure, is localized on top of the riblets, and presents a positive/negative alternation in the streamwise direction. For larger s (see Fig. 14), the influence of the riblets is stronger: the optimal forcing only spans five riblets and appear more undulated. The response has a strong streamwise component localized on top of the riblets. In all cases, the spanwise component takes the form of oblique waves. Lastly, in the case of $s = 4.5$, the forcing wavelength becomes smaller than that of the riblets and now penetrates deeply into the grooves. For all riblet spacing, the Orr mechanism is at play and appears through the realignment in the spanwise direction of the coherent structures. The responses are oblique waves which are likely to trigger oblique transition. The fact that the presence of streamwise riblets induces an optimal forcing in the form of oblique waves is an important (although counterintuitive) observation. This indicates that spatial spacing can trigger three-dimensional features of the flow response even in a setup where the baseflow is two-dimensional. In the context of controlling laminar-turbulent

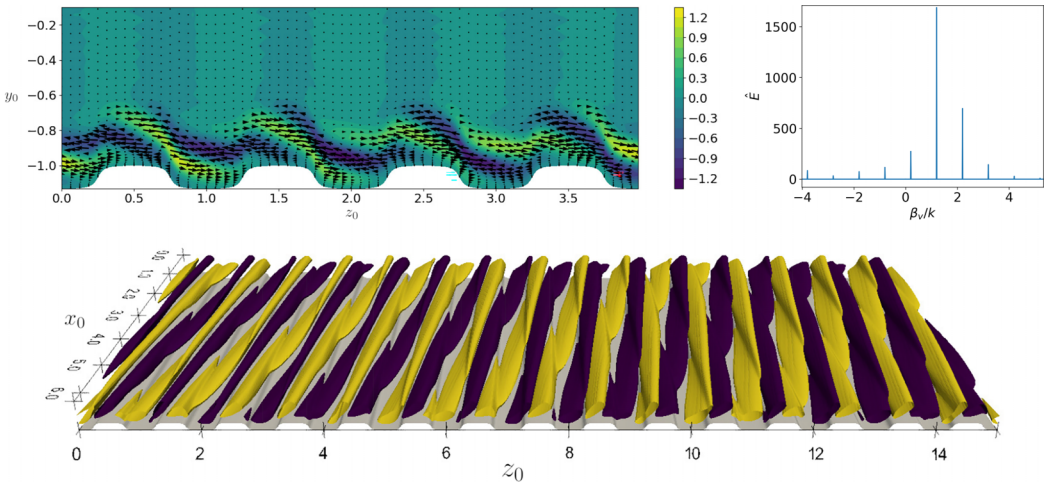

FIG. 14. Same as Fig. 12 for $s = 4.5$.

transition, this observation is very compelling since the onset and development of oblique waves may be problematic. Indeed, because of nonlinearities [73], this type of transition has been found to be quicker and to require smaller initial energy than supercritical or even bypass transition [70,74]. Thus, it is crucial to consider the possibility of the development of three-dimensional oblique waves during bypass transition in a channel flow on streamwise-elongated riblets.

VI. CONCLUSIONS

In this paper, the modal and nonmodal stability of the flow over longitudinal riblets have been investigated. A technique based on the coupling between a two-dimensional stability problem, obtained with a domain transform technique [20,21] and the computational framework introduced by Schmid *et al.* [39] is proposed. This technique, through a Bloch wave formalism, allows the computation of modes with different detuning factors and with wavelengths spanning several riblet spacings at a reasonable numerical cost and is naturally extended to nonmodal stability analyses.

Modal instabilities are found to stem mostly from the deformation of a two-dimensional TS wave as also reported in Moradi and Floryan [20]. In the case of large riblet spacing, the instability arises from a center Squire mode for small streamwise wavenumbers [23]. For larger streamwise wavenumbers, a subharmonic mode was also found to have a similar growth rate than the most unstable, fundamental mode.

Transient growth is investigated and phenomena usually associated with spatially forced systems are observed [75]. Three regimes can be observed: for small riblet spacings s, the presence of the riblets slightly affects the transient energy amplification when detuned perturbations are considered, whereas fundamental (small-wavelength) disturbances are strongly dampened. For intermediate values of s, resonances leading to an increase of transient growth can be observed, at first for detuned instabilities only, and then, as s increases, also for fundamental ones. In particular, it is observed that this resonance is obtained when the riblet wavelength is imposed equal to the optimal streak size in a smooth channel flow. Ultimately, large spacings are associated with a more rapid (although slightly weaker) lift-up mechanism. In this case, the system does not select a unique ground state, which is a condition associated with geometric frustration [45]. This wavenumber lock-in regime arises from a degeneracy of the largest singular value of the exponential operator, which leads to the superposition of the amplification curves for different roots of unity.

Resolvent analysis shows that the presence of riblets leads to the development of oblique waves which may cause a quick transition to turbulence through nonlinear effects. The Orr mechanism also appears to play a prominent role for every configuration. Spanwise-coherent rollers could not be directly retrieved in this analysis. Two reasons may explain this: first, the chosen riblet shape is not optimal for the development of Kelvin-Helmholtz rollers. Indeed, Endrikat *et al.* [14] found that strong wall-normal shear was necessary to trigger the instability and that scalloped or triangular riblets were better suited. Second, the Kelvin-Helmholtz roller could be a specific feature of the turbulent flow and thus requires the use of a mean flow stability framework with turbulent viscosity as in Chavarin and Luhar [10]. Moreover, since interesting analogies can be found between the observed instabilities in a laminar regime and those obtained in a fully turbulent regime around a mean field [10,38], it might be interesting to extend the analysis to the turbulent case.

As a final remark, the fact that the presence of streamwise riblets induces an optimal forcing in the form of oblique waves is an important (although counterintuitive) observation, since it demonstrates that spatial spacing can trigger three-dimensional flow responses even in a two-dimensional setup. In the context of controlling laminar-turbulent transition, this observation is very compelling since the onset and development of oblique waves may be problematic due to their rapid transition, which is triggered for smaller initial energy than supercritical or even bypass transition. Thus, we conclude that it is crucial to consider the possibility of the development of three-dimensional oblique waves as a flow response to forcing also when considering the flow over streamwise-elongated riblets.

Future works will aim at determining the transition scenarios engendered by these modal and nonmodal instabilities. Moreover, the influence of the shape of the riblets will be investigated as

well. Finally, we must say that the numerical approach developed here is in principle not limited to the case of the channel and can be extended to open flows such as a boundary layer. Of course, the results are probably not directly transposable from one flow to another, since the channel flow is homogeneous in the streamwise direction, whereas this is not the case for a boundary layer. Future work will aim at investigating this case, which is most useful for possible practical applications of riblets.

ACKNOWLEDGMENTS

A part of the research was funded by Research Grant No. PRIN 2022 PNRR_-P2022CZ5KZPNRR, "SLIPS: Slippery surfaces for drag reduction," of the Italian Ministery of University and Research (MUR), founded by the European Unit-Next Generation EU.

APPENDIX: DOMAIN TRANSFORMATION

The physical domain $\mathbf{x}_0 = [x_0, y_0, z_0]^T$ is mapped onto a computational domain $\mathbf{x}_1 = [x_1, y_1, z_1]^T$, allowing the numerical treatment of both baseflow and stability problems through spectral collocation methods. The transformation produces extra terms in the Navier-Stokes equations. For the sake of clarity, the transformation [Eq. (4)] is recalled:

$$x_1 = x_0, \quad z_1 = z_0, \quad y_1 = (1-\gamma)y_0 + \gamma, \quad \text{with} \quad \gamma = \eta(z_0)/[\eta(z_0) - 2], \tag{4}$$

where $\eta(z_0) = \epsilon \arctan[2\sin\pi(z_0 - z_b)/\delta_b]/\pi$ is defining the shape of the trapezoidal roughness. Its height is denoted by ϵ while $\delta_b = 0.4$ is a coefficient determining the slope of the roughness. Relations between the derivative operators in the different systems are easily obtained from the chain rule and are given as

$$\frac{\partial}{\partial y_0} = \frac{\partial}{\partial y_1} - \gamma\frac{\partial}{\partial y_1}, \tag{A1}$$

$$\frac{\partial}{\partial z_0} = \frac{\partial}{\partial z_1} + \gamma'(1-y_0)\frac{\partial}{\partial y_1}. \tag{A2}$$

In a similar fashion, second-order derivatives can be obtained:

$$\frac{\partial^2}{\partial y_0^2} = (1-\gamma)^2\frac{\partial^2}{\partial y_1^2}, \tag{A3}$$

$$\frac{\partial^2}{\partial z_0^2} = \frac{\partial^2}{\partial z_1^2} + \gamma''(1-y_0)\frac{\partial}{\partial y_1} + 2\gamma'(1-y_0)\frac{\partial^2}{\partial y_1\partial z_1} + [\gamma'(1-y_0)]^2\frac{\partial^2}{\partial y_1^2}. \tag{A4}$$

Finally, the Laplacian with the new coordinates is defined as

$$\nabla_1^2 = \frac{\partial^2}{\partial y_1^2} + \frac{1}{s^2}\frac{\partial^2}{\partial z_1^2} \tag{A5}$$

$$= (1-\gamma)^2\frac{\partial^2}{\partial y_1^2} + \frac{1}{s^2}\left[\frac{\partial^2}{\partial z_1^2} + \gamma''(1-y_0)\frac{\partial}{\partial y_1} + 2\gamma'(1-y_0)\frac{\partial^2}{\partial y_1\partial z_1} + [\gamma'(1-y_0)]^2\frac{\partial^2}{\partial y_1^2}\right]. \tag{A6}$$

[1] O. Reynolds, III. An experimental investigation of the circumstances which determine whether the motion of water shall be direct or sinuous, and of the law of resistance in parallel channels, Proc. R. Soc. London **35**, 84 (1883).

[2] C. F. Colebrook, Turbulent flow in pipes, with particular reference to the transition region between the smooth and rough pipe laws, J. Inst. Civ. Eng. **11**, 133 (1939).
[3] L. F. Moody, Friction factors for pipe flow, Trans. ASME **66**, 671 (1944).
[4] J. Nikuradse, Laws of Flow in Rough Pipes (1950), NTRS - NASA Technical Report No. nACA TM 1292.
[5] P. Luchini, F. Manzo, and A. Pozzi, Resistance of a grooved surface to parallel flow and cross-flow, J. Fluid Mech. **228**, 87 (1991).
[6] H. Choi, P. Moin, and J. Kim, Direct numerical simulation of turbulent flow over riblets, J. Fluid Mech. **255**, 503 (1993).
[7] R. García-Mayoral and J. Jiménez, Drag reduction by riblets, Philos. Trans. R. Soc. A **369**, 1412 (2011).
[8] R. García-Mayoral and J. Jiménez, Hydrodynamic stability and breakdown of the viscous regime over riblets, J. Fluid Mech. **678**, 317 (2011).
[9] N. Abderrahaman-Elena, C. T. Fairhall, and R. García-Mayoral, Modulation of near-wall turbulence in the transitionally rough regime, J. Fluid Mech. **865**, 1042 (2019).
[10] A. Chavarin and M. Luhar, Resolvent analysis for turbulent channel flow with riblets, AIAA J. **58**, 589 (2020).
[11] Y. Suzuki and N. Kasagi, Turbulent drag reduction mechanism above a riblet surface, AIAA J. **32**, 1781 (1994).
[12] S.-J. Lee and S.-H. Lee, Flow field analysis of a turbulent boundary layer over a riblet surface, Exp. Fluids **30**, 153 (2001).
[13] D. B. Goldstein and T.-C. Tuan, Secondary flow induced by riblets, J. Fluid Mech. **363**, 115 (1998).
[14] S. Endrikat, D. Modesti, R. García-Mayoral, N. Hutchins, and D. Chung, Influence of riblet shapes on the occurrence of Kelvin–Helmholtz rollers, J. Fluid Mech. **913**, A37 (2021).
[15] J. Floryan, Three-dimensional instabilities of laminar flow in a rough channel and the concept of hydraulically smooth wall, Eur. J. Mech. B: Fluids **26**, 305 (2007).
[16] J. M. Floryan, Stability of wall-bounded shear layers in the presence of simulated distributed surface roughness, J. Fluid Mech. **335**, 29 (1997).
[17] J. M. Floryan, Two-dimensional instability of flow in a rough channel, Phys. Fluids **17**, 044101 (2005).
[18] J. Szumbarski and J. M. Floryan, A direct spectral method for determination of flows over corrugated boundaries, J. Comput. Phys. **153**, 378 (1999).
[19] S. Husain and J. Floryan, Spectrally-accurate algorithm for moving boundary problems for the Navier–Stokes equations, J. Comput. Phys. **229**, 2287 (2010).
[20] H. V. Moradi and J. M. Floryan, Stability of flow in a channel with longitudinal grooves, J. Fluid Mech. **757**, 613 (2014).
[21] U. Ehrenstein, On the linear stability of channel flow over riblets, Phys. Fluids **8**, 3194 (1996).
[22] A. Mohammadi and J. M. Floryan, Spectral algorithm for the analysis of flows in grooved channels, Int. J. Numer. Methods Fluids **69**, 606 (2012).
[23] A. Mohammadi, H. Moradi, and J. Floryan, New instability mode in a grooved channel, J. Fluid Mech. **778**, 691 (2015).
[24] P. J. Schmid, Nonmodal stability theory, Annu. Rev. Fluid Mech. **39**, 129 (2007).
[25] P. Luchini, Reynolds-number-independent instability of the boundary layer over a flat surface: Optimal perturbations, J. Fluid Mech. **404**, 289 (2000).
[26] M. Matsubara and P. H. Alfredsson, Disturbance growth in boundary layers subjected to free-stream turbulence, J. Fluid Mech. **430**, 149 (2001).
[27] S. Cherubini, J.-C. Robinet, A. Bottaro, and P. De Palma, Optimal wave packets in a boundary layer and initial phases of a turbulent spot, J. Fluid Mech. **656**, 231 (2010).
[28] M. Landahl, A note on an algebraic instability of inviscid parallel shear flows, J. Fluid Mech. **98**, 243 (1980).
[29] F. Waleffe, On a self-sustaining process in shear flows, Phys. Fluids **9**, 883 (1997).
[30] J. M. Hamilton, J. Kim, and F. Waleffe, Regeneration mechanisms of near-wall turbulence structures, J. Fluid Mech. **287**, 317 (1995).

[31] Y. Hwang and C. Cossu, Self-sustained process at large scales in turbulent channel flow, Phys. Rev. Lett. **105**, 044505 (2010).
[32] E. Reshotko and L. Leventhal, Preliminary experimental study of disturbances in a laminar boundary layer due to distributed surface roughness, in *Proceedings of the14th Fluid and Plasma Dynamics Conference* (AIAA, 1984).
[33] T. C. Corke, A. Bar-Sever, and M. V. Morkovin, Experiments on transition enhancement by distributed roughness, Phys. Fluids **29**, 3199 (1986).
[34] R. S. Downs, E. B. White, and N. A. Denissen, Transient growth and transition induced by random distributed roughness, AIAA J. **46**, 451 (2008).
[35] X. Liu, K. Luo, and J. Fan, Transient growth and receptivity of steady disturbances to irregular rough walls, J. Fluids Eng. **139**, 071202 (2017).
[36] J. Szumbarski and J. M. Floryan, Transient disturbance growth in a corrugated channel, J. Fluid Mech. **568**, 243 (2006).
[37] M. R. Jovanović, From bypass transition to flow control and data-driven turbulence modeling: An input–output viewpoint, Annu. Rev. Fluid Mech. **53**, 311 (2021).
[38] W. Ran, A. Zare, and M. R. Jovanović, Model-based design of riblets for turbulent drag reduction, J. Fluid Mech. **906**, A7 (2021).
[39] P. J. Schmid, M. F. de Pando, and N. Peake, Stability analysis for n-periodic arrays of fluid systems, Phys. Rev. Fluids **2**, 113902 (2017).
[40] G. R. Grek, V. V. Kozlov, and S. V. Titarenko, An experimental study of the influence of riblets on transition, J. Fluid Mech. **315**, 31 (1996).
[41] D. C. Chu and G. E. Karniadakis, A direct numerical simulation of laminar and turbulent flow over riblet-mounted surfaces, J. Fluid Mech. **250**, 1 (1993).
[42] P. Luchini and G. Trombetta, Effects of riblets upon flow stability, Appl. Sci. Res. **54**, 313 (1995).
[43] F. Lynch and M. Klinge, Some practical aspects of viscous drag reduction concepts, SAE Tech. Pap. 912129 (1991).
[44] P. J. Schmid and L. Brandt, Analysis of fluid systems: Stability, receptivity, sensitivity, Appl. Mech. Rev. **66**, 024803 (2014).
[45] M. Nixon, E. Ronen, A. A. Friesem, and N. Davidson, Observing geometric frustration with thousands of coupled lasers, Phys. Rev. Lett. **110**, 184102 (2013).
[46] J. R. Philip, Flows satisfying mixed no-slip and no-shear conditions, J. Appl. Math. Phys. (ZAMP) **23**, 353 (1972).
[47] F. Picella, J.-C. Robinet, and S. Cherubini, Laminar–turbulent transition in channel flow with superhydrophobic surfaces modelled as a partial slip wall, J. Fluid Mech. **881**, 462 (2019).
[48] H. V. Moradi and J. M. Floryan, Maximization of heat transfer across micro-channels, Int. J. Heat Mass Transfer **66**, 517 (2013).
[49] J. M. Floryan and M. Asai, On the transition between distributed and isolated surface roughness and its effect on the stability of channel flow, Phys. Fluids **23**, 104101 (2011).
[50] V. Theofilis, Global linear instability, Annu. Rev. Fluid Mech. **43**, 319 (2011).
[51] T. Tatsumi and T. Yoshimura, Stability of the laminar flow in a rectangular duct, J. Fluid Mech. **212**, 437 (1990).
[52] L. N. Trefethen, *Spectral Methods in MATLAB*, Software, Environments and Tools (Society for Industrial and Applied Mathematics, Philadelphia, 2000).
[53] K. H. Yu, C. J. Teo, and B. C. Khoo, Linear stability of pressure-driven flow over longitudinal superhydrophobic grooves, Phys. Fluids **28**, 022001 (2016).
[54] S. D. Tomlinson and D. T. Papageorgiou, Linear instability of lid- and pressure-driven flows in channels textured with longitudinal superhydrophobic grooves, J. Fluid Mech. **932**, A12 (2022).
[55] S. A. Orszag, Accurate solution of the Orr–Sommerfeld stability equation, J. Fluid Mech. **50**, 689 (1971).
[56] M. Asai and J. Floryan, Experiments on the linear instability of flow in a wavy channel, Eur. J. Mech. B: Fluids **25**, 971 (2006).
[57] H. Ho and M. Asai, Experimental study on the stability of laminar flow in a channel with streamwise and oblique riblets, Phys. Fluids **30**, 024106 (2018).

[58] A. Jouin, N. Ciola, S. Cherubini, and J.-C. Robinet, Detuned secondary instabilities in three-dimensional boundary-layer flow, Phys. Rev. Fluids **9**, 043901 (2024).
[59] T. Herbert, Secondary instability of plane channel flow to subharmonic three-dimensional disturbances, Phys. Fluids **26**, 871 (1983).
[60] L. M. Mack, A numerical study of the temporal eigenvalue spectrum of the Blasius boundary layer, J. Fluid Mech. **73**, 497 (1976).
[61] C. E. Grosch and H. Salwen, The continuous spectrum of the Orr-Sommerfeld equation. Part 1. The spectrum and the eigenfunctions, J. Fluid Mech. **87**, 33 (1978).
[62] L. Brandt, The lift-up effect: The linear mechanism behind transition and turbulence in shear flows, Eur. J. Mech. B: Fluids **47**, 80 (2014).
[63] P. J. Schmid and D. S. Henningson, *Stability and Transition in Shear Flows*, Applied Mathematical Sciences (Springer-Verlag, New York, 2001).
[64] L. H. Gustavsson, Energy growth of three-dimensional disturbances in plane Poiseuille flow, J. Fluid Mech. **224**, 241 (1991).
[65] S. C. Reddy and D. S. Henningson, Energy growth in viscous channel flows, J. Fluid Mech. **252**, 209 (1993).
[66] R. Schmitz and W. Zimmermann, Spatially periodic modulated Rayleigh-Bénard convection, Phys. Rev. E **53**, 5993 (1996).
[67] M. Z. Hossain and J. M. Floryan, Instabilities of natural convection in a periodically heated layer, J. Fluid Mech. **733**, 33 (2013).
[68] M. Hossain and J. Floryan, Wavenumber lock-in and spatial parametric resonance in convection, J. Fluid Mech. **944**, A47 (2022).
[69] B. J. McKeon and A. S. Sharma, A critical-layer framework for turbulent pipe flow, J. Fluid Mech. **658**, 336 (2010).
[70] S. J. Chapman, Subcritical transition in channel flows, J. Fluid Mech. **451**, 35 (2002).
[71] W. F. Orr, The stability or instability of the steady motions of a perfect liquid and of a viscous liquid, Proc. R. Ir. Acad., Sect. A **27**, 9 (1907).
[72] Y. Jiao, Y. Hwang, and S. I. Chernyshenko, Orr mechanism in transition of parallel shear flow, Phys. Rev. Fluids **6**, 023902 (2021).
[73] P. J. Schmid and D. S. Henningson, A new mechanism for rapid transition involving a pair of oblique waves, Phys. Fluids **4**, 1986 (1992).
[74] A. Lundbladh, D. S. Henningson, and S. C. Reddy, Threshold amplitudes for transition in channel flows, in *Transition, Turbulence and Combustion: Volume I Transition*, edited by M. Y. Hussaini, T. B. Gatski, and T. L. Jackson (Springer, 1994), pp. 309–318.
[75] R. Manor, A. Hagberg, and E. Meron, Wave-number locking in spatially forced pattern-forming systems, Europhys. Lett. **83**, 10005 (2008).